High-speed Digital Imaging and Computational Modeling of Hybrid Metal-Composite Plates Subjected to Water-based Impulsive Loading

S. Avachat[1] · M. Zhou[1]

Abstract The response of hybrid metal/composite plates subjected to water-based impulsive loads is analyzed using experiments and computations. The analysis focuses on the effect of varying material properties on load-carrying capacity, deflection, impulse transmission, energy dissipation and damage. The three structural designs studied are unmodified monolithic aluminum plates, unmodified monolithic composite plates and hybrid metal/composite laminates. The plates are circumferentially clamped and subjected to transverse, out-of-plane impulses of varying intensities. The experiments are supported by fully dynamic numerical simulations using a Coupled Eulerian–Lagrangian (CEL) framework which accounts for fluid–structure interactions and damage and failure in the constituent materials. Results show that load intensity determines the deformation and failure modes. The monolithic composite plates exhibit large-scale in-ply cracking, delamination and shear rupture near the clamped edges, while the aluminum plates undergo plastic deformation and petalling. The hybrid metal/composite structures show superior blast-resistance than both types of monolithic plates in terms of failure loads and energy dissipation, with the stacking sequence of the composite and metal layers significantly influencing the behavior.

✉ M. Zhou
min.zhou@gatech.edu

[1] The George W. Woodruff School of Mechanical Engineering, School of Materials Science and Engineering, Georgia Institute of Technology, Atlanta, GA 30332-0405, USA

Introduction

Marine vessels operate in severe environmental conditions involving temperature extremes, dynamic loads and corrosive sea water. In addition to operational loads, the structures are also required to withstand hydrodynamic impulsive loads due to surface and sub-surface blasts and weapons impact. The deformation response of plates under water-based impulsive loads is of great importance in the design of blast-resistant marine structures for naval applications. Fluid structure interaction (FSI) effects play an important role in determining the dynamic response and can be exploited to improve the blast mitigation capability of the structures.

Early studies pertaining to the response of metallic plates subjected to transverse impulsive loads was carried out by Hudson [1] and Wang and Hopkins [2] who developed theoretical models for dynamic plasticity under blast loads. Experiments and simulations involving impulsively-loaded steel plates have revealed a range of deformation mechanisms and failure modes primarily dependent on load intensity [3, 4]. At low values of incident impulse, the plates experience bending and stretching without rupture, exhibiting a primarily Mode I deformation response. At intermediate values of

incident impulse, plate stretching occurs, followed by tensile necking and Mode II rupture near the supports. Theoretical studies by Lee and Wierzbicki [5, 6] have revealed discing and petalling deformation modes that resemble Mode II failure. Experimental studies involving explosive impulsive loads carried out by Balden and Nurick [7] have revealed shear rupture mode of failure (Mode III). Kazemahvazi et al. [8] analyzed the underwater blast response of axisymmetrically clamped copper plates and confirmed the dependence of failure modes on impulse intensity, concluding that failure modes are highly sensitive to peak pressure but relatively insensitive to blast decay time.

In recent years, composite materials have been employed in naval construction and the off-shore industry. As a consequence, understanding the response of composite structures to high intensity underwater impulsive loads has gained importance. Many investigations have been carried out on the dynamic deformation and failure of layered materials. Most of the studies on sandwich composites have focused on low velocity contact-based loads due to drop weight and projectile impact [9–15]. Results show that key damage mechanisms include matrix cracking, fiber breakage and interlaminar delamination. The primary driving forces for the damage processes are transverse shear stresses [16–18]. Interlaminar delamination is the most detrimental to stiffness and strength and, therefore, is a major concern because delamination is not visible on the surface. Chang and co-workers [19–21] have studied the damage behavior of composite laminates under low velocity impact loading, concluding that in-ply matrix cracking precedes delamination growth and shear and bending crack initiation. The damage behavior of composite laminates is significantly influenced by matrix material, composite layup and geometric aspects such as size, thickness and loading area [22–24]. Minnaar and Zhou [25] used a novel interferometric experimental setup to show that interlaminar crack speeds are significantly higher under shear loading, and that crack speeds are strongly influenced by loading rate in mode II. However, only limited study has been reported on the dynamic response of composites to water-based impulsive loads. Analyses have primarily focused on sandwich structures because such structures offer considerably high shear and bending stiffness to weight ratios than homogeneous plates of equivalent mass. Experiments and computations focusing on different core topologies and specimen sizes have been carried out by Espinosa and co-workers [26–28] and McShane et al. [29] using underwater pressure impulses generated by gas gun impact and by Dharmasena et al. [30] using planar pressure impulses generated by explosive sheets. Battley and co-workers developed a high-speed servo-hydraulic testing system and concluded that slamming impacts on a deformable sandwich panels result in different peak and residual pressures to those from a rigid panels [31, 32]. Shukla and co-workers [33–37] examined the dynamic response of

sandwich structures consisting of woven E-glass composite facesheets and stitched core to air-based shock loading and concluded that stitched cores exhibit superior mechanical performance. A combined experimental and computational analysis of the response to underwater blast by Avachat and Zhou [38] has revealed that sandwich structures significantly outperform monolithic structures at all impulsive levels and environmental conditions including air-backed and water-backed structures. Additionally, a balance of core stiffness and softness provides optimal blast resistance by allowing load spreading and energy dissipation while mitigating the effects of localized core compressive failure and rupture.

Although polymer matrix composites are finding increasing applications in marine applications due to their high strength-to-weight ratios and fatigue and corrosion resistance, these materials may have lower impact resistance and higher cost of manufacturing in comparison to metallic structures. In recent years, hybrid material systems combining composites and metals have been developed in order to symbiotically provide superior stiffness, strength and impact resistance in comparison to either monolithic composite or metallic structures. Fiber-Metal Laminate (FML) concepts such as GLARE (Glass Laminate Aluminum Reinforced Epoxy), CARALL (Carbon fibre Reinforced Aluminum Laminate) and ARALL (Aramid fiber Reinforced Aluminum Laminate) are finding applications in aircraft due to their superior blast and impact resistance [39]. Seyed Yaghoubi and Liaw [40–42] performed an experimental and computational analysis of the ballistic response of GLARE FMLs and showed that cross-ply composites dissipate more energy than unidirectional composites. Fatt et al. [43] showed that energy dissipation was primarily governed by out-of-plane bending in ballistic impact of clamped GLARE panels. High-velocity impact experiments performed by Abdullah and Cantwell [44] demonstrated that energy dissipation is highly dependent on stretching during flexure in metallic layers which perform independently of composite layers. Fan et al. [45] performed low-velocity impact testing of GLARE FMLs which show enhancement in penetration resistance with increasing composite layer thickness. Langdon et al. [46, 47] analyzed the response of FMLs to blast loading, revealing a number of failure modes in the form of perforation of aluminum and composite layers, debonding between aluminum layers and shear failure in composite plates. Finite element simulations on impulsively loaded FMLs highlight the need for accurate modelling of the blast loading and accounting for 3D constitutive behavior of each constituent of the hybrid structures [48–51].

Despite recent interest in the mechanical response of hybrid metal-composite structures, especially their behavior under blast loading, there are a number of unresolved issues. Specifically, only limited studies have been reported on the behavior of both monolithic and hybrid plates subjected to

water-based impulsive loading [27, 29, 52]. Since there are significant differences in air-blasts and water-blasts, understanding the response of hybrid structures under water-based impulsive loading is of critical importance in the design of marine structures. Independently assessing the performance of composite and metallic plates subjected to high-intensity underwater impulsive loads is essential for accurately delineating the response of each component. Additionally, the role of stacking sequence and the relative positioning of composite and metallic layers in the hybrid structure has not been analyzed. Finally, the deformation and failure of hybrid plates subjected to underwater impulsive loads are complicated due to fluid–structure interaction (FSI) effects, competing damage mechanisms, complex failure modes, interfacial effects and material heterogeneity and, therefore, require a physically-based multiphysics computational framework in order for each of the aspects to be accounted for.

The objective of this combined experimental and computational analysis is to characterize the behavior of monolithic and hybrid plates subjected to underwater impulsive loads and delineate the role of FSI, material properties, interfacial effects and stacking sequence in determining the structural response. The focus is on quantifying the damage and deformation in axis-symmetrically clamped plates subjected to impulsive load of a range of intensities and identifying structural configurations that enhance blast resistance. Previous studies involving hybrid structures have focused on FMLs manufactured using alternating layers of composites and metals. Since the role of individual layers in structural response is unclear, the hybrid plates in this analysis have bilayer configurations consisting of only two layers of respective materials. The configurations allow the delineation of the effects of stacking sequence of the constituent layers on response.

The impulsive loads are generated using a recently developed experimental setup called the Underwater Shock Loading Simulator (USLS) and mimic the high-pressure, exponentially-decaying impulses observed in underwater explosions. As shown in Fig. 1, the USLS consists of a projectile-impact-based impulsive loading system, a water chamber, a target holder and a safety enclosure. A range of load intensity with durations between 300 and 1000 μs and peak pressures up to 100 MPa is generated. The impulses are measured using high-dynamic-range-piezoelectric pressure transducers (#109C11 manufactured by PCB Inc.) and a high-frequency data acquisition system from National Instruments Inc. (NI-4432). *In-situ* measurements of the material response are obtained using high-speed digital imaging and force transducers, providing an opportunity to assess the role of core density and strength on blast resistance during events mimicking an underwater detonation. A Coupled Eulerian–Lagrangian (CEL) 3D numerical model is used to complement the experiments. This combined experimental and computational approach allows the comparison and validation of constitutive and damage models and is expected to reveal insights into the deformation processes in the blast-loaded plates.

Specimen construction

Four different structural configurations are studied. Firstly, monolithic aluminum plates are manufactured from 1100 aluminum alloy and have a thickness of 0.812 mm and an areal mass of 2.19 kg/m^2. Secondly, monolithic composite plates are manufactured from quasi-isotropic carbon-fiber/epoxy laminates and have a thickness of 1.58 mm and an areal mass of 2.31 kg/m^2. The aluminum plates are denoted as "AL" and carbon-fiber/epoxy plates are denoted as "CF" respectively. Finally, hybrid plates are constructed by stacking a 0.406 mm thick aluminum plate and a 0.82 mm thick composite plate in the form of bi-layers bonded with West System 105 epoxy resin. Based on the stacking sequence, the hybrid plates are classified into two types: (1) stacking sequence with aluminum on the impulse side and carbon-fiber/epoxy on the distal side (denoted as "AL/CF") and (2) stacking sequence with carbon-fiber/epoxy on the impulse side and aluminum on the distal side (denoted as "CF/AL"), both with an areal mass of 2.42 kg/m^2 including the mass of the adhesive. The different materials and section thicknesses of the specimens studied are summarized in Table 1. The similar areal masses of the different structural configurations enables comparison of their dynamic deformation and blast resistance on an equal mass basis.

The composite laminates are manufactured by curing carbon-fiber epoxy prepregs under vacuum. The prepreg system consists of VTM 264 epoxy resin system from Cytec Industries Inc. cured at 65 to 120 °C and impregnated with continuous unidirectional carbon fibers of an areal weight of 300 g per square meter (GSM) from Tenax. The thickness of each cured lamina is 0.3 mm and the laminas are stacked in a quasi-isotropic (0/-45/45/90)$_s$ layup to obtain the required thickness in each case. In hybrid structures, the laminas are stacked in the (0/-45/45/90) sequence until the required mass is achieved. In the finite element simulations, each unidirectional lamina is simulated explicitly to accurately represent the behavior of the entire carbon-fiber/epoxy laminate and capture damage and deformation. The epoxy layers between two laminas, also called "resin rich layers", are modeled using cohesive elements to capture interfacial fracture and delamination. Details about the computational approach are provided in "Numerical model" section.

Instrumented underwater impulsive loading apparatus

Gas gun impact has been successfully used to generate impulsive loading through water [27, 52–55]. To obtain controlled

Fig. 1 Schematic illustration of the Underwater Shock Loading Simulator (USLS) for axisymmetrically clamped thin plates. Pictured are the gas reservoir, gun barrel, water chamber, modular support system, specimen and the Imacon 200D high-speed camera
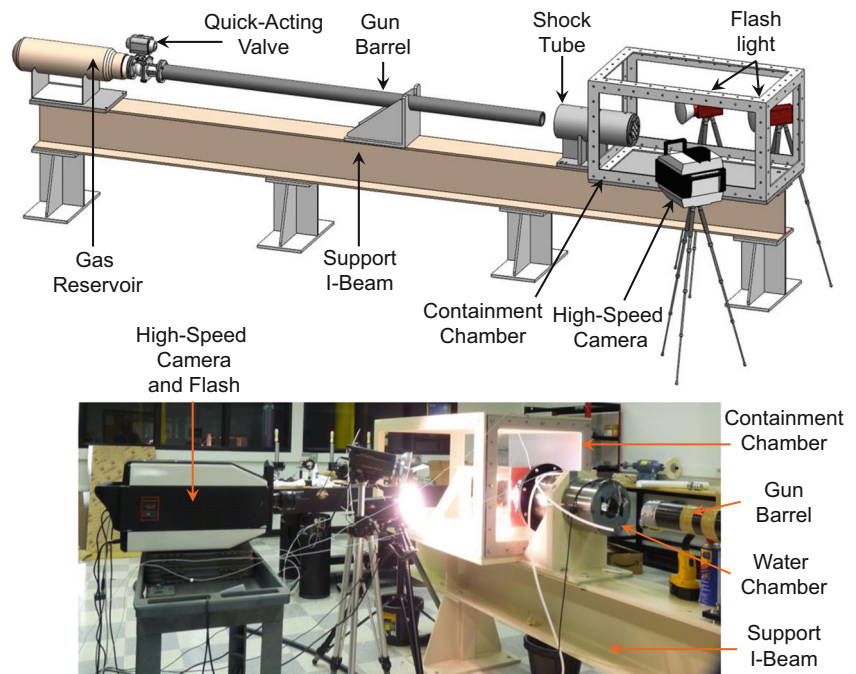
loading and simulate different water-structure contact conditions, the Underwater Shock Loading Simulator (USLS) in Fig. 1 is designed to provide a variety of loading configurations with quantitative diagnostics [53–55]. Important features of this facility include the ability to generate water-based impulsive loading of a wide range of intensity, the ability to simulate the loading of submerged structures, and integrated high-speed photographic and laser interferometric diagnostics. The impulsive load that impinges on the target induces deformation in the specimen at strain rates up to 10^4 s^{-1}. Projectile impact velocities in the range of 15–150 ms^{-1} are used to delineate the effect of loading rate on the deformation and failure behavior of the structures analyzed. This velocity range corresponds to peak pressures between 15 and 200 MPa, which are comparable to pressures observed in underwater explosions [56–59].

The experimental results reported in this study are obtained from high-speed digital imaging of the deformation response of the impulsively loaded plates. The high-speed camera used is an Imacon 200D digital camera which is capable of recording digital images at framing rates up to 200×10^6 frames per second at a resolution of 1360×1024 pixels per frame. For the purposes of this analysis, the framing rate used is approximately 5000 frames per second. Figure 2 shows a schematic illustration of the cross-section of the USLS. The shock tube (or anvil) is a horizontally mounted 500 mm long steel cylinder with an inside diameter of 76 mm. The shock tube is filled with water with a piston plate mounted at the front end and the specimen at the rear end. A projectile is accelerated by the gas gun and strikes the piston plate, generating a planar pressure pulse in the shock tube. The length and diameter of the projectile are 80 mm and 76 mm, respectively, while the length and diameter of the piston are 60 mm and 88 mm, respectively. The specimen is 200 mm in diameter and is axisymmetrically clamped with a collar with an internal diameter of 125 mm and an external diameter of 200 mm and 8 equally-spaced bolts as shown in Fig. 2. A circular region 76 mm in diameter is subjected to a transverse, spatially uniform underwater impulsive load, resulting in out-of-plane deflection. Since a collar is used to secure the specimen to the shock tube, it can be assumed that the plate is securely clamped with no relative

Table 1 Specimens studied. The thicknesses of the different sections are varied to maintain similar areal masses in the hybrid metal-composite structures

Plate	Plate designation	Aluminum section thickness (mm)	Composite section thickness (mm)	Areal mass (kg/m^2)
Monolithic aluminum	AL	0.812	0	2.19
Monolithic composite	CF	0	1.58	2.31
Hybrid plate	AL/CF	0.406	0.82	2.42
Hybrid plate	CF/AL	0.406	0.82	2.42

Fig. 2 A schematic illustration of the loading mechanism in the Underwater Shock Loading Simulator (USLS) showing the loading configuration used to evaluate the blast resistance of axisymmetrically clamped plates
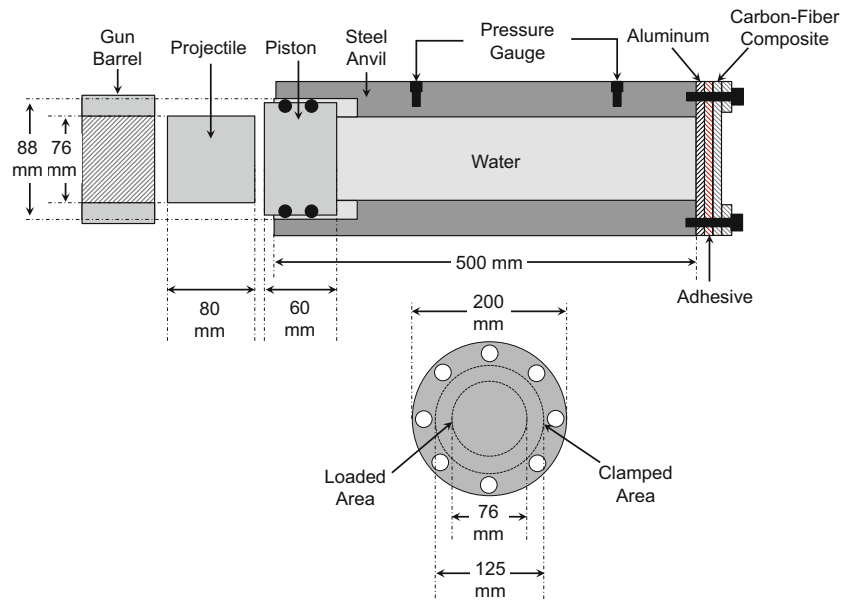
motion or friction between the portion of the plate between the clamping ring and water tube. There are two pressure sensors on the shock tube. The first pressure sensor is located at a distance of 152 mm, while the second sensor is located at a distance of 228 mm from the opening of the shock tube. The experimental pressure pulses in Fig. 3 are those measured by the second sensor.

According to Taylor's analysis of one dimensional blast waves [60] impinging on a light, rigid, free standing plate, the pressure in the fluid at a distance r from an explosive source follows the relation

$$p(t) = p_0 \exp\left(-\frac{t}{t_0}\right), \tag{1}$$

where p_0 is the peak pressure, t is time and t_0 is the pulse time on the order of milliseconds. The area under the pressure–time curve is the impulse carried by the wave and is given by

$$I_0 = \int_0^t p(t)\, dt = p_0 t_0. \tag{2}$$

For a free standing plate of areal mass m, the impulse transferred to the plate is

$$\frac{I_T}{I_0} = \psi^{\left(\frac{\psi}{1-\psi}\right)}, \tag{3}$$

where ψ is the fluid–structure interaction (FSI) parameter given by

$$\psi = \frac{\rho_w c_w t_0}{m}, \tag{4}$$

and ρ_w is the density of water and c_w is the speed of sound in water. This FSI parameter is an important

aspect of Taylor's analysis because it helps to delineate the effects of a pressure pulse applied instantaneously *versus* the effects of a pressure pulse decaying over a certain time period.

It has been shown that this FSI effect can be exploited to improve the blast mitigation capability of structures subjected to transient loads [61, 62].

For the current analysis, a non-dimensionalized incident impulse $\bar{I}$ in the form of

$$\bar{I} = \frac{I_0}{\rho_w c_w \sqrt{A}} \tag{5}$$

is used, where A is the area under loading. The experiments and numerical modeling for different $\bar{I}$ values simulate the effects of different standoff distances from an explosive source. Swisdak [60, 63, 64] showed that for an underwater explosion using a Tri Nitro Toluene (TNT) explosive source, there exists a power-law relation between the mass M of the explosive and peak pressure p_0 (in MPa) such that

$$p_0 = 52.4 \left(\frac{M^{1/3}}{r}\right)^{1.13}, \tag{6}$$

where r is the standoff distance in meters. In the experiments reported here, pressures ranging from 10 MPa to 300 MPa can be generated using different projectile velocities. Figure 3 shows the comparison of experimentally measured and numerically calculated pressure histories corresponding to four different projectile velocities. The resulting impulses in each pressure pulse are plotted on the secondary axis of these plots. The rise time of the pressure pulses is on the order of 25 μs and the decay time is on the order of 1500 μs. The impulsive loads have peak pressures of 56, 110, 160, 198 MPa which approximately correspond to

Fig. 3 Experimentally measured and numerically calculated pressure histories in the water chamber for four different levels of impulse magnitude ($\bar{I}$)
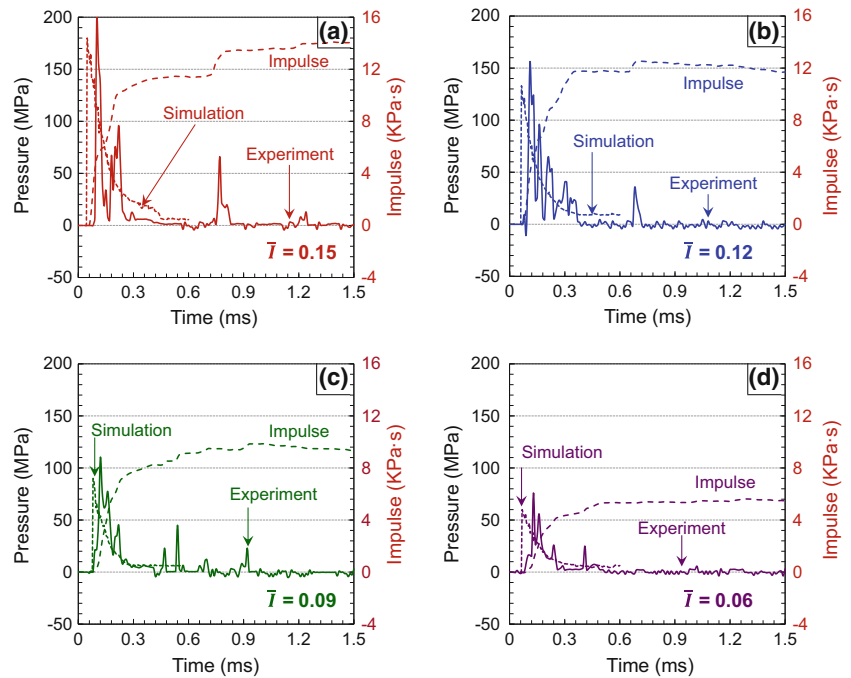
100 kg of TNT detonating at distances of 4.5, 2.4, 1.7 and 1.4 m, respectively. The incident impulse magnitudes are $I = \int_0^t p(t)dt =$ 5.48, 9.33, 11.70 and 14.05 kPa·s and the normalized impulse magnitudes calculated using equation (5) are $\bar{I} \approx$ 0.15, 0.12, 0.09, 0.06 respectively.

Numerical model

Modeling of water-structure interaction

The model consists of a Lagrangian domain for the solids and an Eulerian domain for the water. In the Lagrangian domain, nodes are fixed within the material and nodal displacements track the material deformation. Since each Lagrangian element is always 100 % within a single material, the material boundary coincides with element boundaries. In contrast, Eulerian the domain consists of nodes that are fixed in space and the material flows through the elements that do not experience deformation. Eulerian elements may also be partially or completely void, allowing material to flow into empty space, capturing cavitation, a crucial aspect of fluid flow. Materials tracked by Eulerian elements can interact with Lagrangian elements through Eulerian–Lagrangian contact algorithms to allow fully coupled multiphysics simulations like fluid–structure interactions. This Coupled Eulerian–Lagrangian (CEL) framework allows the severe deformation in water and the FSI to be captured. In addition to simulating the blast wave propagation in the USLS, the Eulerian formulation also captures the exponentially decaying pressure waves and resulting cavitation at the fluid–structure interface. The interaction between the water and structure is effected by tying the nodes in the water to the corresponding nodes of the structure, thereby ensuring continuity of displacements when contact occurs.

The response of water in the Eulerian domain is described by the Mie-Grüneisen equation of state

$$p = \frac{\rho_0 c_0^2 \eta}{(1-s\eta)^2}\left(1 - \frac{\Gamma_0 \eta}{2}\right) + \Gamma_0 \rho_0 E_m, \qquad (7)$$

where p is pressure, c_0 is the speed of sound, ρ_0 is initial density, E_m is internal energy per unit mass, Γ_0 is Grüneisen's Gamma at a reference state, $s = dU_s/dU_p$ is the Hugoniot slope coefficient, U_s is the shock wave velocity, and U_p is particle velocity which is related to U_s through a linear Hugoniot relation

$$U_S = c_0 + sU_p. \qquad (8)$$

The parameters for the Mie-Grüneisen equation of state are listed in Table 2. The space enclosed by the shock-tube is prescribed the properties of water while the space that is outside the shock-tube is kept as a "void", allowing water to flow into it as a result of high-pressure wave impinging on the target. This has the effect of instantaneously relieving the pressure in the water-

Table 2 Parameters for the Mie-Gruneisen equation of state for water

Parameter	Symbol	Unit	Value
Density of water	ρ	kg/m^3	1000
Speed of sound in water	c	m/s	1482
Gruneisen's Gamma	Γ_0	–	0.1

chamber in a manner consistent with experimental observations. In the case of specimen rupture, the CL framework allows water to flow out of the breached portion.

Constitutive and damage models for aluminum

The metal plates studied here are made of 1100 aluminum alloy. It is highly resistant to seawater and industrial chemicals and has a relatively high yield strength, high strain hardening and high ductility. The Johnson-Cook model [65] which accounts for strain-hardening, thermal softening, and strain rate dependence is used to describe the material's response. Specifically,

$$\overline{\sigma}\left(\overline{\varepsilon}^{pl}, \dot{\varepsilon}^{pl}, \theta\right) = \left[A + B\left(\overline{\varepsilon}^{pl}\right)^n\right]\left[1 + C\ln\left(\frac{\dot{\varepsilon}^{pl}}{\dot{\varepsilon}_0}\right)\right]\left[1 - \left(\hat{\theta}\right)^m\right], \quad (9)$$

where $\overline{\sigma}$ is the Mises equivalent stress, $\overline{\varepsilon}^{pl}$ is the equivalent plastic strain, $\dot{\varepsilon}^{pl}$ is the equivalent plastic strain rate, and A, B, C, m and n are material parameters measured at or below the transition temperature, $\theta_{transition}$, $\dot{\varepsilon}_0$ is a reference strain rate, and $\hat{\theta}$ is the non-dimensional temperature defined as

$$\hat{\theta} \equiv \begin{cases} 0, & \text{for} \quad \theta < \theta_{transition}; \\ (\theta - \theta_{transition})/(\theta_{melt} - \theta_{transition}), & \text{for} \quad \theta_{transition} \leq \theta \leq \theta_{melt}; \quad \text{and} \\ 1, & \text{for} \quad \theta > \theta_{melt}. \end{cases}$$
$$(10)$$

In the above expressions, θ is the current temperature, θ_{melt} is the melting temperature and $\theta_{transition}$ is the transition temperature below which the yield stress is independent of the temperature. When the temperature exceeds the melting temperature, the material behaves like a fluid and has no shear resistance. The use of the Johnson–Cook constitutive model partly reflects the nature of the deformations analyzed and partly reflects the fact that extensive experimental data is available and has been used to calibrate this model for the conditions analyzed. Indeed, there are more "sophisticated" models than the Johnson–Cook model. These models use different parameters or internal stare variables to deal with issues such as complicated loading paths, varying stress triaxiality, and deformation mechanisms. However, the key aspects of the loading conditions analyzed in this paper are dynamic, rate-dependent, monotonic (no unloading considered), and approximately proportional. Under such conditions, the constitutive response of the steels considered here can be well-characterized as dependent on strain, strain rate and temperature. Models using relations between stress and these quantities are effectively similar or equivalent, as long as enough parameters exist to allow a good fit to experimental data. Another way to look at it is that, for the conditions stated above, many more sophisticated models using, say, certain internal state variables (ISVs) essentially simplify to relations

involving stress, strain, strain rate and temperature as independent variables.

The failure model is based on the value of equivalent plastic strain. The damage parameter, ω, is defined as

$$\omega = \sum\left(\frac{\Delta\overline{\varepsilon}^{pl}}{\overline{\varepsilon}_f^{pl}}\right), \quad (11)$$

where $\Delta\overline{\varepsilon}^{pl}$ is an increment of the equivalent plastic strain, $\overline{\varepsilon}_f^{pl}$ is the strain at failure, and the summation is performed over all increments up to the hitherto state in the analysis. The strain at failure is assumed to be dependent strain rate and temperature such that

$$\overline{\varepsilon}_f^{pl} = \left[D_1 + D_2\exp\left(-D_3\frac{p}{\overline{\sigma}}\right)\right]\left[1 + D_4\ln\left(\frac{\dot{\overline{\varepsilon}}^{pl}}{\dot{\varepsilon}_0}\right)\right][1 + D_5],$$
$$(12)$$

where D_1, D_2, D_3, D_4, and D_5, are experimentally determined damage parameters, $p = -\sigma_{ii}/3$ is the hydrostatic pressure. The values the parameters are obtained from Johnson and Cook [65], Raftenberg [66] and Corbett [67] and are shown in Table 3.

Constitutive and damage models for composite laminates

A finite-deformation framework is adopted to account for large deformations in the composite. Linear orthotropic elastic constitutive behavior is assumed. Damage initiation and failure of each composite ply are captured with Hashin's damage model [68, 69]. This is a homogenized model so that individual fibers and

Table 3 Parameters for the Johnson-Cook constitutive and damage model for aluminum [65, 67]

Parameter	Symbol	Unit	Value
Density	ρ	kg/m^3	2700
Young's modulus	E	GPa	70
Poisson's ratio	υ	-	0.33
Johnson-Cook constant	A	MPa	324
Johnson-Cook constant	B	MPa	113
Johnson-Cook constant	C	-	0.002
Johnson-Cook constant	m	-	1.34
Johnson-Cook constant	n	-	0.42
Melting temperature	θ_{melt}	°C	1200
Reference temperature	θ	°C	25
Johnson-Cook constant	D_1	-	−0.77
Johnson-Cook constant	D_2	-	1.45
Johnson-Cook constant	D_3	-	0.47
Johnson-Cook constant	D_4	-	0.00
Johnson-Cook constant	D_5	-	1.60

fiber-matrix interfaces are not modeled explicitly. Rather, the model provides a phenomenological representation of the different damage modes in composite structures. This framework incorporates four damage mechanisms: (1) matrix damage in tension, (2) matrix damage in compression, (3) fiber damage in tension, and (4) fiber damage in compression. The damage criteria for these mechanisms use the following parameters,

(1) matrix tension ($\widehat{\sigma}_{22} \geq 0$):

$$F_m^T = \left(\frac{\widehat{\sigma}_{22}}{T_{22}}\right)^2 + \left(\frac{\widehat{\tau}_{12}}{S_{12}}\right)^2, \tag{13}$$

(2) matrix compression ($\widehat{\sigma}_{22} < 0$):

$$F_m^C = \left(\frac{\widehat{\sigma}_{22}}{2S_{23}}\right)^2 + \left(\frac{\widehat{\tau}_{12}}{S_{12}}\right)^2 + \left[\left(\frac{C_{22}}{2S_{23}}\right)^2 - 1\right]\frac{\widehat{\sigma}_{22}}{C_{22}}, \tag{14}$$

(3) fiber tension ($\widehat{\sigma}_{11} \geq 0$):

$$F_f^T = \left(\frac{\widehat{\sigma}_{11}}{T_{11}}\right)^2 + \left(\frac{\widehat{\tau}_{12}}{S_{12}}\right)^2, \text{and} \tag{15}$$

(4) and fiber compression ($\widehat{\sigma}_{11} < 0$):

$$F_f^C = \left(\frac{\widehat{\sigma}_{11}}{C_{11}}\right). \tag{16}$$

In the above expressions, subscript "11" denotes the longitudinal direction and subscript "22" denotes the transverse direction, E, T and C are the tensile modulus, tensile strength and compressive strength, respectively. The in-plane/longitudinal shear strengths are $S_{12}=S_{31}$ while the out-of-plane/transverse shear strength is S_{23}. In addition, $\widehat{\sigma}_{11}$, $\widehat{\sigma}_{22}$ and $\widehat{\tau}_{12}$ are components of the effective stress tensor in the form of $\widehat{\sigma} = M\sigma$, with σ being the nominal stress tensor and M being the damage operator given by

$$M = \begin{bmatrix} 1/(1-D_f) & 0 & 0 \\ 0 & 1/(1-D_m) & 0 \\ 0 & 0 & 1/(1-D_s) \end{bmatrix}, \tag{17}$$

where D_f, D_m, and D_s are damage variables in fibers, matrix and associated with the shear modes, respectively [70].

In Equations (13)-(15), for each parameter, a value of less than 1.0 indicates no damage and a value of 1.0 indicates damage. The upper bound to all damage variables in an element is $D_{max}=1$. Prior to damage initiation, the material is linear elastic. After damage initiation, the response of the material follows

$$\sigma = C_d\varepsilon, \tag{18}$$

where ε is the strain and C_d is the elasticity matrix accounting for damage in the form of

$$C_d = \frac{1}{D}\begin{bmatrix} (1-D_f)E_{11} & (1-D_f)(1-D_m)v_{21}E_{11} & 0 \\ (1-D_f)(1-D_m)v_{12}E_{22} & (1-D_m)E_{22} & 0 \\ 0 & 0 & (1-D_m)\mu D \end{bmatrix}. \tag{19}$$

In the above relation, $D=1-(1-D_f)(1-D_m)v_{12}v_{21}$, D_f reflects the current state of fiber damage, D_m reflects the current state of matrix damage, D_s reflects the current state of shear damage, E_{11} is the Young's modulus of the composite in the fiber direction, E_{22} is the Young's modulus of the composite in the transverse directions, μ is the shear modulus, v_{12} and v_{21} are Poisson's ratios. The components of the damage variables are

$$\left.\begin{array}{l} D_f = \begin{cases} D_f^t, \text{fiber tensile damage variable,} \\ D_f^c, \text{fiber compressive damage variable,} \end{cases} \\ D_m = \begin{cases} D_m^t, \text{matrix tensile damage variable,} \\ D_m^c, \text{matrix compressive damage variable, and} \end{cases} \\ D_s = 1-\left(1-D_f^t\right)\left(1-D_f^c\right)\left(1-D_m^t\right)\left(1-D_m^c\right). \end{array}\right\} \tag{20}$$

D_f^t, D_f^c, D_m^t, and D_m^c are calculated using G_{mt}^c, G_{mc}^c, G_{ft}^c and G_{fc}^c which are fracture energies associated with matrix tension and compression and fiber tension and compression, respectively. The material properties for unidirectional

carbon-fiber/epoxy composite used in these calculations were obtained from Chan et al. [71] and Pinho et al. [72] and are listed in Table 4.

Cohesive finite element framework

The cohesive finite element method (CFEM) has been extensively used to study a wide variety of issues related to delamination and fracture such as tensile decohesion (Needleman [73]), quasi-static crack growth (Tvergaard and Hutchinson[74]), ductile fracture (Tvergaard and Needleman [75, 76]), dynamic fracture (Xu and Needleman [77]), dynamic fragmentation (Camacho and Ortiz [78], Espinosa et al. [79]), delamination in composites (Camanho et al. [80], Minnaar and Zhou [81]) and microstructural fracture (Zhai and Zhou [82]). Here, cohesive elements are specified at the interfaces between individual laminas in the composite structure as well as the interfaces between the aluminum and composite sections in the hybrid plates. The cohesive elements allow damage initiation and development in the interlaminar

Table 4 Material properties for unidirectional carbon-fiber/epoxy laminates [71, 72]

Parameter	Symbol	Unit	Value
Density	ρ	kg/m^3	1580
Longitudinal tensile modulus	E_{11}	MPa	138,000
Transverse tensile modulus	E_{22}	MPa	9650
Shear modulus	G_{12}	MPa	5240
Shear modulus	G_{13}	MPa	5240
Longitudinal tensile strength	T_{11}	MPa	2280
Longitudinal compressive strength	C_{11}	MPa	1440
Transverse tensile strength	T_{22}	MPa	57
Transverse compressive strength	C_{22}	MPa	228
Shear strength	S_{12}	MPa	71
Shear strength	S_{13}	MPa	71
Shear strength	S_{23}	MPa	71

regions to be captured. A bilinear traction-separation law is adopted to describe the behavior of the cohesive elements [80]. The linear-elastic part of the traction-separation law relates the traction vector $\mathbf{t}$ to the element stiffness $\mathbf{K}$ and the separation $\mathbf{u}$ resulting from the traction vector $\mathbf{t}$. This relationship is given by

$$\mathbf{t} = \mathbf{Ku}. \tag{21}$$

The above equation can be expressed in matrix form to indicate coupling between the normal and shear components of the traction-separation relationship, i.e.,

$$\begin{pmatrix} t_n \\ t_s \\ t_t \end{pmatrix} = \begin{bmatrix} K_{nn} & K_{ns} & K_{nt} \\ K_{ns} & K_{ss} & K_{st} \\ K_{nt} & K_{st} & K_{tt} \end{bmatrix} \begin{pmatrix} u_n \\ u_s \\ u_t \end{pmatrix}. \tag{22}$$

Full coupling between normal and shear components in the traction-separation response is represented by the off-diagonal terms. For the purposes of this work, an uncoupled relation is chosen, i.e.,

$$\begin{pmatrix} t_n \\ t_s \\ t_t \end{pmatrix} = \begin{bmatrix} K_{nn} & 0 & 0 \\ 0 & K_{ss} & 0 \\ 0 & 0 & K_{tt} \end{bmatrix} \begin{pmatrix} u_n \\ u_s \\ u_t \end{pmatrix}. \tag{23}$$

Although the linear-elastic part of the response has no coupling between shear and normal components, damage initiation and evolution have a mixed-mode form. Damage initiation follows the quadratic interaction relationship shown in equation (23), where t_n is the normal stress in a cohesive element, t_s is the shear stress, and t_n^0 and t_s^0 are the critical values of t_n and t_s, respectively, which represent the respective cohesive strengths. In this paper, t_s^0 and t_t^0 are assumed to have the same value. Because it is not physically meaningful for compressive tractions to contribute to damage initiation, only non-negative (tensile) normal tractions are considered in the

damage initiation rule. This is indicated by the presence of the Macaulay brackets around t_n. Specifically, damage is initiated when

$$\left(\frac{\langle t_n \rangle}{t_n^0} \right)^2 + \left(\frac{t_s}{t_s^0} \right)^2 + \left(\frac{t_t}{t_t^0} \right)^2 = 1. \tag{24}$$

A schematic representation of the bilinear traction-separation law is shown in Fig. 4. Loading initially proceeds from point A to B, at which point softening occurs with increasing separation until failure. Once damage is initiated in a cohesive element, the interface follows the mixed-mode fracture criterion of Benzeggagh and Kenane given in equation (24) [83]. In this relationship, G_n, G_s and G_t are the work performed by tractions t_n, t_s and t_t respectively. G_n^C, G_s^C and G_t^C are the critical fracture energies in the normal and shear directions, respectively. These quantities are used to determine the degree of damage in a cohesive surface pair. For convenience, the critical fracture energies in the two shear directions are treated as equal (i.e., $G_s^C = G_t^C$). The criterion is written as

$$G_n^C + \left(G_s^C - G_n^C \right) \left(\frac{G_s + G_t}{G_n + G_s + G_t} \right) = G^C. \tag{25}$$

The parameters for all cohesive relations used are obtained from the work performed by Lapczyk and Hurtado [70] and are presented in Table 5. The traction-separation stiffness for cohesive elements along interfaces between the laminas is 10^3 times the stiffness of the corresponding bulk elements. This choice has two benefits. First, artificial softening of the model is avoided. Second, the work of separation associated with the linear-elastic portion of the cohesive behavior is minimized, ensuring that the bulk of the work is in the fracture energy, providing adequate softening in the cohesive response. Although the method of constituent preparation can have a significant influence on the resulting composite fracture toughness [84], only a single set of interface properties are considered in this paper.

After failure of cohesive elements, contact between element faces is considered in the model using the a contact algorithm similar to that developed by Camacho and Ortiz
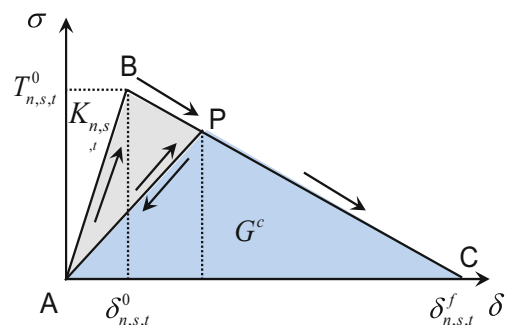

Fig. 4 Bi-linear law for cohesive traction-separation behavior

Table 5 Material properties for epoxy [70]

Parameter	Symbol	Unit	Value
Normal stiffness	K_n	MPa	2,000,000
Shear stiffness	K_s, K_t	MPa	2,000,000
Critical normal traction	t_n^0	MPa	50
Critical shear traction	t_s^0, t_t^0	MPa	50
Critical normal fracture energy	G_n^C	N/mm	4.0
Critical shear fracture energy	G_s^C, G_t^C	N/mm	4.0

[78]. The algorithm identifies free surfaces and fractured surfaces as potential contact surfaces in each time step of the simulation. Nodal coordinates at the end of every time step are used to define master and slave surfaces for the next time step. Nodal displacements are then calculated at the beginning of every time step. The corresponding nodal coordinates are used to check whether nodes of one internally defined surface have penetrated another internally defined surface. If penetration is predicted, then penalty forces of sufficient magnitude are applied to the surfaces in the direction of their normal such that there is contact between them but no interpenetration.

The failure criteria associated with the Johnson-Cook damage model, Hashin damage model and cohesive traction-separation are based on critical values of strain or separation. Failure is predicted when the damage operator in the respective case reaches unity. Once a criterion is satisfied, the properties of failed elements are modified so that only compressive stresses can be supported. Predictions of damage and structural response based on such failure criteria are inherently mesh-size dependent and require a separate length scale for solution convergence, as shown by Needleman and Tvergaard [76] and Gullerud et al. [85]. To resolve this issue, a characteristic length scale L_E is introduced in ABAQUS. For 3-D elements, L_E is the cube-root of element volume. A parametric study is carried, with $w = 100$ μm to 1200 μm. Figure 5(a) shows the energy dissipation through plastic deformation in aluminum plates and Fig. 5(b) shows the peak stress at supports as function of mesh size. The results indicate that the energy dissipated through plastic

deformation is relatively insensitive to mesh size and converges as the mesh is refined. As shown in Fig. 5(b), the solution convergence takes shape toward $w = 500$ μm. This is the size used in the analysis reported here. The handling of mesh size related size scale here is similar to that proposed by Pijaudier-Cabot and Bazant [86] and Comi [87].

Results and discussion

The effect of material properties, stacking sequences, load intensity and loading condition on blast resistance are analyzed experimentally and computationally. The temporal evolution of selected performance metrics as functions of load intensity and material properties are obtained. In particular, the performance metrics studied in detail are out-of-plane deflection, impulse transmission and energy dissipation. Failure modes are evaluated qualitatively to facilitate comparison of dynamic behavior of the different structures. The results for the monolithic structures are first discussed, followed by the results for the hybrid metal/composite structures. The experimental results are used to calibrate the computational model and evaluate response over a wide range of loading and structural attributes.

Experimental results and numerical validation

Figure 3 shows a comparison of experimentally measured and numerically calculated pressure histories in the water chamber for four different projectile velocities and impulse magnitudes. Figure 6 shows a cross-sectional view of the finite element model of the USLS with a pressure pulse traveling through the water chamber and impinging upon the clamped specimen. The experimentally measured and calculated pressure pulses show good agreement in terms of peak pressures and decay times. The experimentally measured profiles show slightly faster wave attenuation than the calculated profiles. Clearly, the coupled Eulerian–Lagrangian framework and the Mie-Gruneisen equation

Fig. 5 (a) Energy dissipated through plastic deformation; and (b) averaged peak stress at supports as a function of element size in monolithic aluminum plate for $\bar{I} = 0.12$
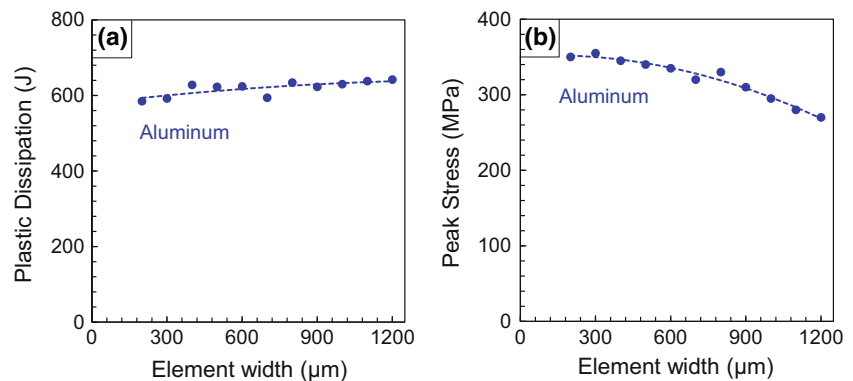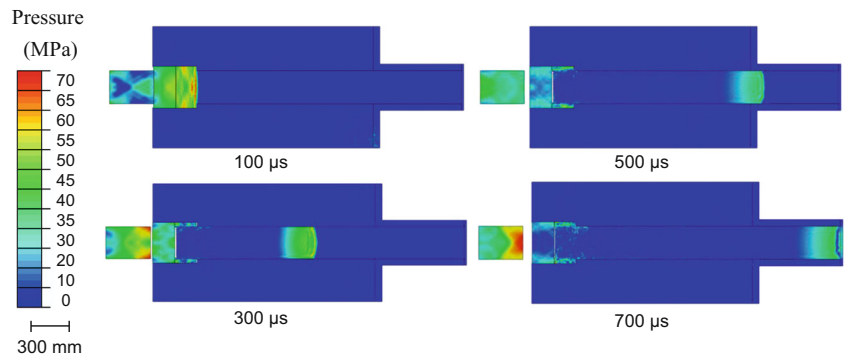
Fig. 6 Cross-sectional view of the USLS load chamber from a finite element simulation showing the distributions of pressure at different locations for an impulsive wave generated with a projectile velocity of 70 ms^{-1} ($\bar{I}=$ 0.12)

of state allow most essential features of the loading pulses in the experiments to be captured.

Figure 7 shows a comparison of high-speed digital photographs and corresponding computational results of the deformation of a monolithic aluminum plate subjected to loading at $\bar{I}=0.12$. The calculated images show the damage distributions in the material. After the onset of loading, the aluminum plate experiences out-of-plane deflection with the maximum deformation occurring in the central region. At $t=600$ μs, three cracks initiate and extend outward towards the supports, leading to "petalling" failure at $t=1000$ μs. The experiment and simulation are in agreement in terms of failure mode and overall progression of the deformation. Figure 8 shows experimental images of and corresponding calculated contour plots of Hashin damage parameter in a carbon-fiber/epoxy laminate plate subjected to loading at $\bar{I}=0.12$. Maximum deformation is observed near the supports in both the experiment and the simulation. Since carbon-fiber/epoxy composite plates have high stiffness, the impulse causes the axisymmetrically clamped plate to undergo shear-dominated deformation and failure near the clamped region. This behavior is in sharp contrast to the bulging and tensile cracking observed in the aluminum plates. The differing deformation and failure behaviors of the metal and composite plates offer an opportunity for their unique strengths to be combined.
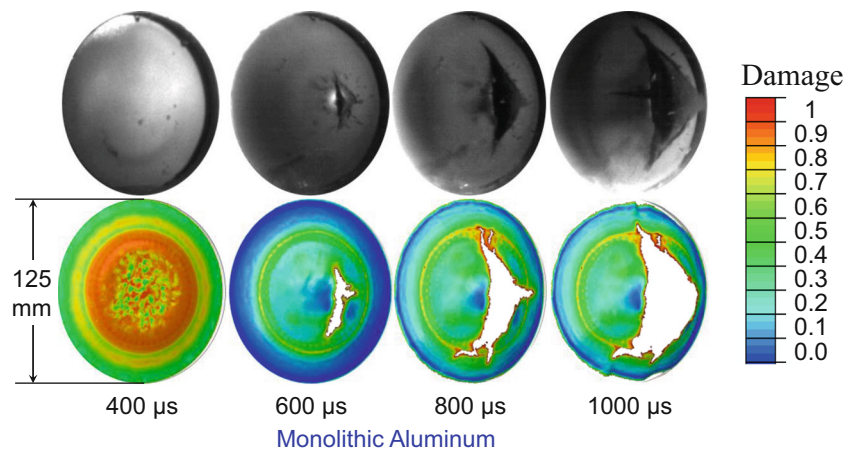
Figure 9 shows experimental images and calculated contour plots for the damage of a hybrid metal/composite plate at the same load intensity as that in Figs. 7 and 8. The stacking sequence is aluminum/carbon-fiber/epoxy, with the aluminum on the impulse side and the composite on the distal side. The deformation is initially through out-of-plane deflection in the aluminum plate (see, e.g., $t=400$ μs) and shear near the support in the composite plate (see, e.g., $t=600$ μs). The bulging in the aluminum plate causes the composite to fail at two locations: near the clamped support and the central region. The impulse breaches the plate at $t=800$ μs, causing tensile necking and fracture in the aluminum plate and cracking in the composite plate. Figure 10 shows experimental images and calculated contour plots for the damage of a hybrid with a stacking sequence of carbon-fiber/epoxy/aluminum, with the composite on the impulse side and the aluminum on the back side. At $t=400$ μs, the deformation in the hybrid plate is rather uniform, involving regions of high stresses in the central region and near the clamped boundary. At $t=600$ μs, the deformation is localized in a small region near the center and near the edge of the clamped periphery. Most importantly, this plate does not experience failure seen in the other three cases already discussed.

Figure 11(a-c) shows the post-mortem images of monolithic aluminum plates, aluminum/carbon-fiber/epoxy plates and

Fig. 7 A comparison of experimentally observed and numerically calculated deformation fields with damage distribution at different times for a monolithic aluminum plate subjected to $\bar{I}=0.12$.

Fig. 8 A comparison of experimentally observed and numerically calculated deformation fields with damage distribution at different times for a monolithic carbon fiber/epoxy composite plate subjected to $\bar{I}=$ 0.12.

Monolithic Composite
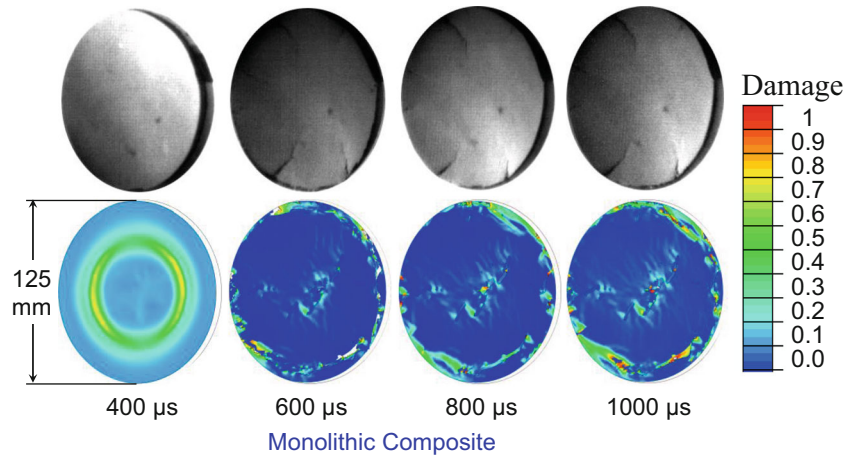
carbon-fiber/epoxy/aluminum plates recovered after the test. The monolithic composite plates fail due to shear cracking and fragmentation and, therefore, are not especially informative and are not included. The deformation modes in monolithic aluminum plates at different incident load intensities clearly illustrate the effects of loading rate. At $\bar{I}=0.06$, the monolithic plate experiences out-of-plane deflection and bulging while the hybrid plates experience relatively minor out of plate deflection. At $\bar{I}=0.09$, the bulging in the aluminum plate is more severe and causes rupture near the clamped periphery. For the

Fig. 9 A comparison of experimentally observed and numerically calculated deformation fields with damage distribution at different times for a hybrid plate with the (AL/CF) stacking sequence) subjected to $\bar{I}=0.12$.
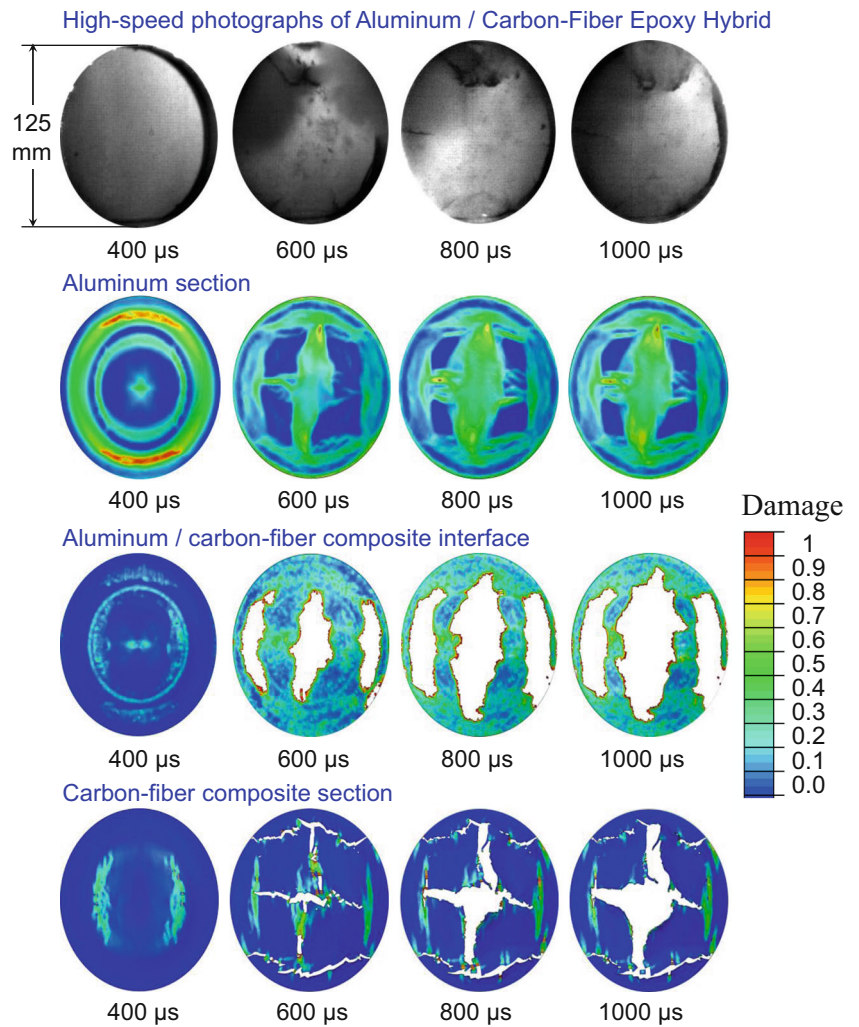

High-speed photographs of Aluminum / Carbon-Fiber Epoxy Hybrid

Aluminum section

Aluminum / carbon-fiber composite interface

Carbon-fiber composite section

Fig. 10 A comparison of experimentally observed and numerically calculated deformation fields at different times for a hybrid plate with the (CF/AL) stacking sequence subjected to $\bar{I} = 0.12$.
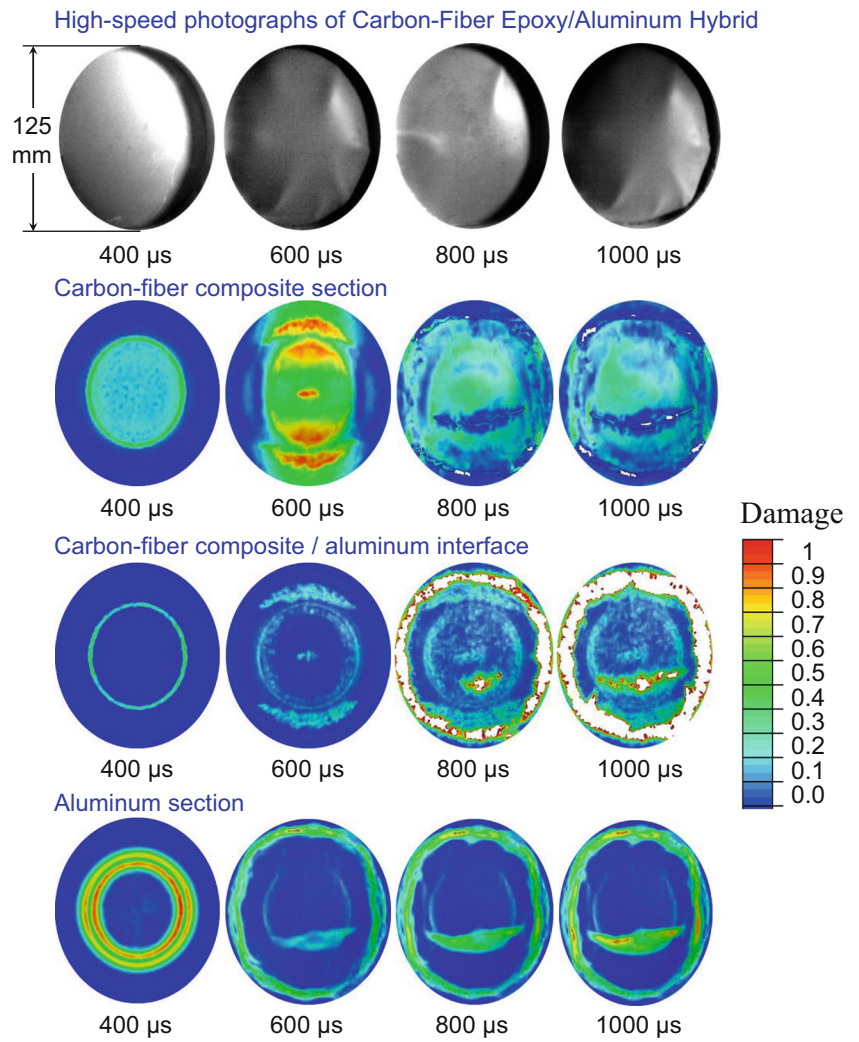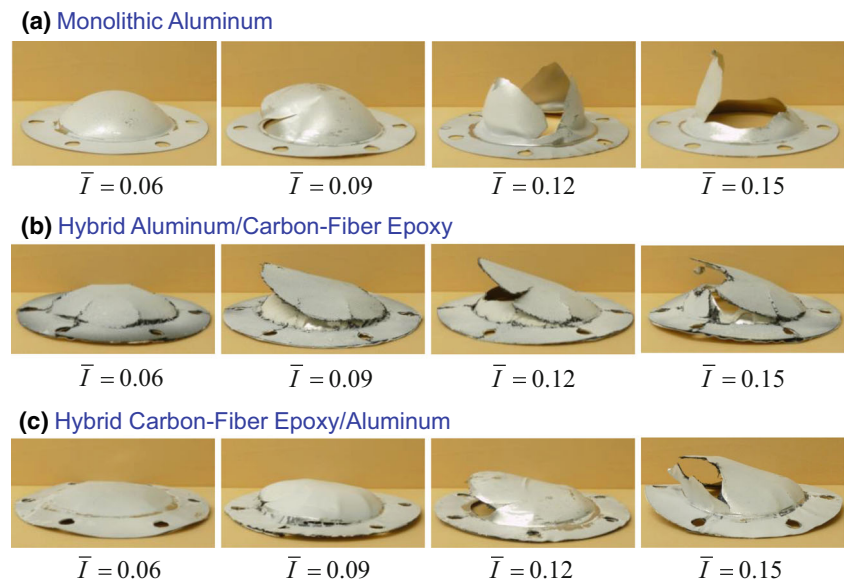

High-speed photographs of Carbon-Fiber Epoxy/Aluminum Hybrid

125 mm

400 µs   600 µs   800 µs   1000 µs

Carbon-fiber composite section

400 µs   600 µs   800 µs   1000 µs

Carbon-fiber composite / aluminum interface

400 µs   600 µs   800 µs   1000 µs

Aluminum section

400 µs   600 µs   800 µs   1000 µs

Damage
1
0.9
0.8
0.7
0.6
0.5
0.4
0.3
0.2
0.1
0.0

Fig. 11 Post-mortem photographs of impulsively loaded (**a**) monolithic aluminum; (**b**) hybrid (AL/CF) and (**c**) hybrid (CF/AL) plates for different incident impulse intensities. Since monolithic composite plates exhibit fragmentation, post-mortem images for these plates are not shown

(a) Monolithic Aluminum

$\bar{I} = 0.06$ $\bar{I} = 0.09$ $\bar{I} = 0.12$ $\bar{I} = 0.15$

(b) Hybrid Aluminum/Carbon-Fiber Epoxy

$\bar{I} = 0.06$ $\bar{I} = 0.09$ $\bar{I} = 0.12$ $\bar{I} = 0.15$

(c) Hybrid Carbon-Fiber Epoxy/Aluminum

$\bar{I} = 0.06$ $\bar{I} = 0.09$ $\bar{I} = 0.12$ $\bar{I} = 0.15$

same load intensity, the (AL/CF) hybrid plate exhibits bulging and shear rupture of the distal composite plate while the (CF/AL) hybrid plate experiences significantly less deflection and does not show failure in either the aluminum or composite sections. At $\bar{I}$=0.12, the monolithic aluminum plate experiences petalling failure with rupture initiating at the center and propagating towards the support to create three petals as shown in Fig. 7. The (AL/CF) hybrid plate undergoes tensile failure in the metallic section and shear failure in the distal composite section. The (CF/AL) hybrid plate primarily fails due to boundary effects and stress concentrations near the axisymmetrically clamped edge. At $\bar{I}$=0.15, the aluminum plate fails due to tensile stresses and both hybrid plates exhibit rupture originating near the central region and propagating towards to the support.

At all impulse levels considered in this analysis, the structural response of the monolithic composite laminates consists of shear cracking near the axisymmetrically clamped boundary and failure is primarily in the form of delamination throughout the plate, matrix cracking near the clamped edges and rupture. The structural response of the aluminum plates is dependent on load intensity but fracture in all cases occurs through tensile stretching. At low load intensities, the aluminum plates exhibit bulging but no rupture; at medium intensities, the aluminum plates undergo petalling failure and rupture; and at high load intensities, the aluminum plates experience localized failure. The results indicate that the response of the hybrid plates is governed by the layup. In the AL/CF plate (with the aluminum section on the impulse side), when the aluminum section bulges, the out-of-plane deflection creates high stresses in the carbon fiber laminate at the center of the plate, leading to significant delamination between the two sections. Conversely, in the CF/AL plate, the carbon fiber composite section prevents the out-of-plane bulging in the aluminum section while the aluminum section prevents shear cracking in the carbon fiber composite section, resulting in a symbiotic effect that enhances blast mitigation at all load intensities while reducing delamination between the two sections. The hybrid plates are mildly sensitive to incident load intensity (primarily because of the aluminum section) and exhibit similar deformation modes at all load intensities.

Figure 12(a) and (b) shows the scanning-electron microscope (SEM) micrographs of fractured aluminum plates subjected to $\bar{I}$=0.12 and $\bar{I}$=0.15 respectively. The images show plastic deformation at ~45° to the loading plane, indicating that rupture occurred in tension due to necking. Since the aluminum plates subjected to $\bar{I}$=0.06 and $\bar{I}$=0.09 experienced dynamic bulging and rupture near the supports, we conclude that the mode of failure for monolithic aluminum plates is tensile in nature for all incident impulse levels studied. Figure 13 reveals that, in contrast to the aluminum plates, the composite laminates exhibit large-scale delamination and shear-dominated in-ply cracking resulting from matrix damage, fiber rupture and fiber-matrix debonding. The

combination of aluminum plates and carbon-fiber/epoxy laminates poses an interesting problem in terms of failure analysis due to the significantly different failure mechanisms in each section. Figure 14(a) and (b) shows SEM micrographs of hybrid plates with stacking sequences (AL/CF) and (CF/AL) respectively. In both cases, failure in the aluminum sections is in the form of mixed-mode fracture resulting from a combination of shear and stretching. Failure in the carbon-fiber/epoxy laminates is consistent with that observed in the monolithic plates, involving large-scale delamination and shear-dominated in-ply cracking near the support. It is instructive to note that the computational model captures these deformation modes and failure mechanisms in both the metallic and composite sections, and at the interfaces.

Out-of-plane deflection

The time-and-space resolved deformation response of the impulsively-loaded plates is evaluated by tracking the out-of-plane deflection, transmitted impulse and energy dissipated cumulatively as well as in each individual component. The maximum values of each performance metric are then compared to evaluate the effect of material properties and stacking sequence on blast resistance. Figure 15(a) shows the out-of-plane displacements of different plates as a function of time with the dotted lines representing the permanent out-of-plane displacements for each plate for $\bar{I}$=0.15. The results reveal that initially, the deflection in the composite plate increases at the highest rate but is surpassed by the deflection in the aluminum plate at t=200 μs. This can be attributed to the high stiffness of the carbon-fiber/epoxy laminate which arrests the deformation of the plate. On the other hand, the aluminum plate undergoes severe plastic deformation and experiences ~15 % higher overall deflection. Both hybrid plates exhibit superior blast resistance, with the (AL/CF) plate undergoing ~70 % of the deflection and the (CF/AL) plate undergoing 50 % of the deflection experienced by the monolithic aluminum plate, respectively. The results also reveal a slight difference (~10 %) between the permanent out-of-plane deflection in the experiments and the peak displacements in simulations, especially for the hybrid structures. This can be attributed to the elastic recovery in the unloading process. Figure 15(b) shows the velocity acquired by each plate under $\bar{I}$=0.15, revealing that the hybrid plates achieve steady-state before both monolithic plates. The peak displacements at t=1200 μs for all structural configurations are shown in Figure 15(c). At low incident impulsive loads, the deflections in monolithic aluminum and composite plates are comparable, while at high incident impulsive loads, the aluminum plates exhibit higher out-of-plane deflection. At all impulsive loads considered, the hybrid plates undergo significantly lower deflection than the monolithic plates, with the (CF/AL) plate showing superior blast resistance in comparison to the (AL/CF) plate.
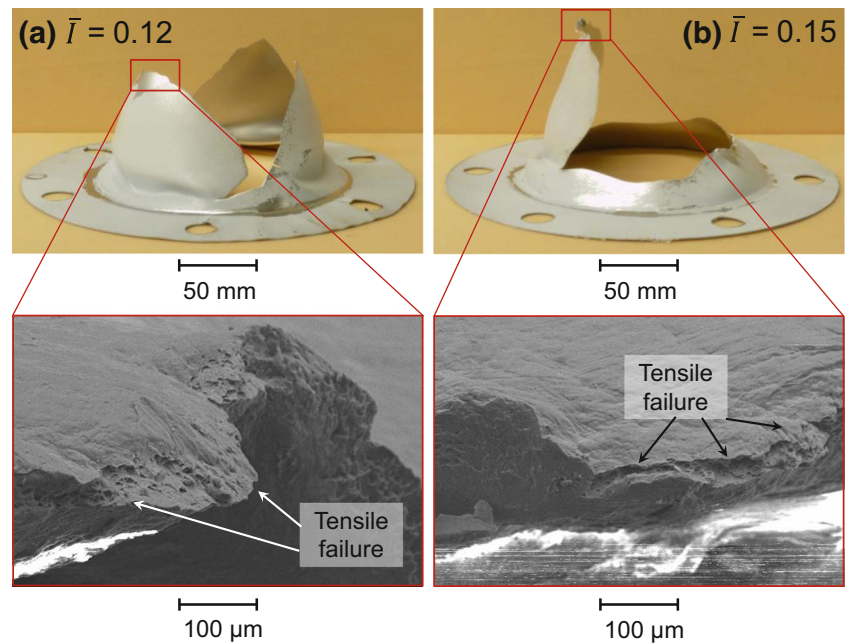
Impulse transmission

A major concern in the design of protective structures is the magnitude of the impulse transmitted through the structures. In evaluating the blast resistance of the monolithic and hybrid plates, the forces and impulses transmitted to the supports can provide an in-depth understanding of the blast mitigation capability. Figure 16(a) and (b) shows the reaction forces measured at supports and the corresponding impulses transmitted by each structure for $\bar{I}$=0.15. The reaction force histories show that the carbon-fiber/epoxy laminate transmits the highest reaction forces and impulses to the supports because of high stiffness and comparatively low areal mass. After an initial peak, the composite plate reaction forces subside over 1000 μs due to a combination of fragmentation and strain recovery. The monolithic aluminum plate continues to deform plastically up to failure and transmits a relatively uniform reaction force. The hybrid plates exhibit an initial peak in transmitted forces followed by strain recovery in both the carbon-fiber/epoxy and aluminum sections. This initial peak

surpasses the peak reaction forces transmitted by the aluminum plate but subsides much more rapidly in comparison to the aluminum plate. The transmitted impulse histories show that hybrid plates transmit significantly lower impulses than the composite plate, with the (AL/CF) plate transmitting 70 % and (CF/AL) plate transmitting 60 % of the impulse transmitted by the carbon-fiber/epoxy laminate, respectively. The impulses transmitted by the hybrid plates and the monolithic aluminum plate are rather similar at all incident loads.

Energy dissipation

When an impulsive wave interacts with a structure, a number of energy dissipation mechanisms are activated. It is important to understand how the dissipation is distributed in the structures in order to determine effectiveness. A significant fraction of the incident energy is dissipated through plastic deformation via tensile stretching in the aluminum plates, as shown in Figure 12. In composite plates, the energy dissipation primarily occurs through interlaminar delamination and in-ply

Fig. 13 Scanning electron microscope (SEM) micrographs at different magnifications for a fractured monolithic composite plate subjected to $\bar{I}$=0.15
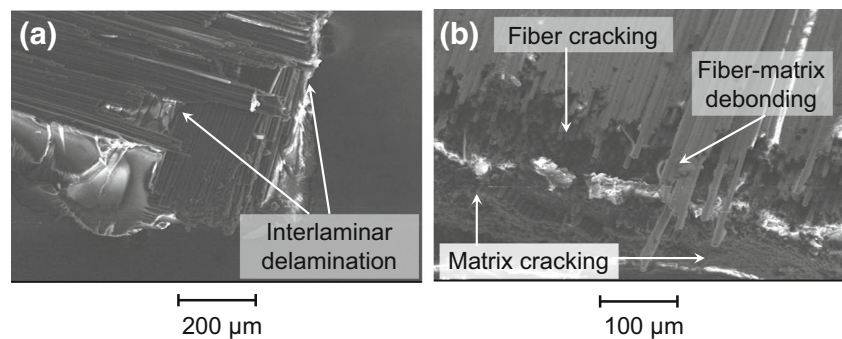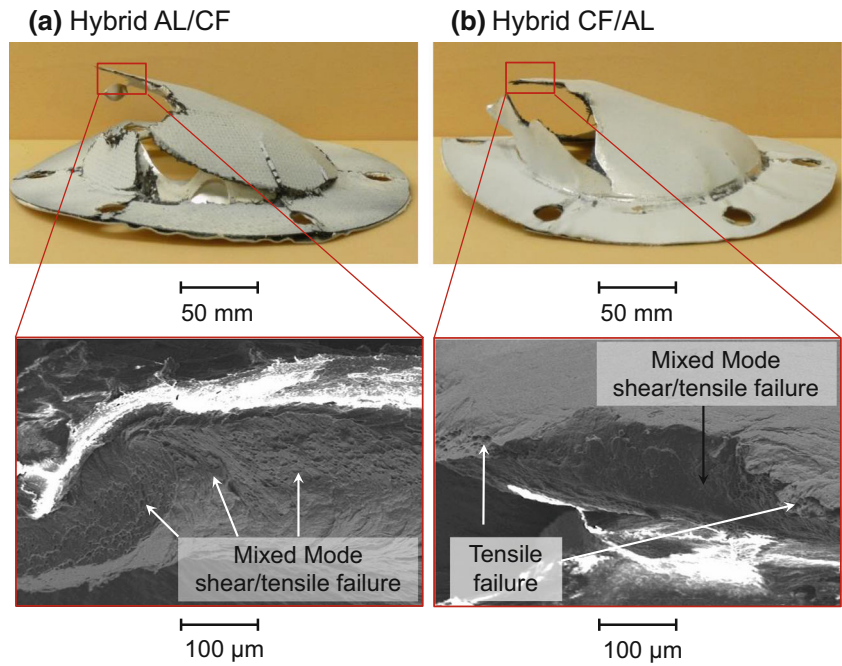
Fig. 14 Scanning electron microscope (SEM) micrographs of fractured hybrid metal composite plates with different stacking sequences: (**a**) hybrid (AL/CF); and (**b**) hybrid (CF/AL). $\bar{I}=0.15$ for both cases

(a) Hybrid AL/CF

50 mm

Mixed Mode shear/tensile failure

100 µm

(b) Hybrid CF/AL

50 mm

Mixed Mode shear/tensile failure

Tensile failure

100 µm

damage in the form of matrix cracking, fiber cracking and fiber-matrix debonding, as shown in Fig. 13. Figure 17(a-d) shows the histories of the energy dissipated in the different components of each structure subjected to $\bar{I}=0.15$. As expected, the aluminum plates exhibit considerably higher energy dissipation in comparison to the composite laminates. Specifically, plastic deformation

in the aluminum plates enables them to dissipate 500 % more energy than the composite plates. Within the composite plate, interlaminar damage dissipation surpasses in-ply damage dissipation. The hybrid plates dissipate similar amounts of total energy with minor differences in the component-level dissipation. Specifically, in the hybrid (AL/CF) plate, the aluminum section

Fig. 15 Computational results for (**a**) out-of-plane displacement and (**b**) mid-plane velocity as functions of time; and (**c**) peak out-of-plane displacements for different structures and incident impulsive loads
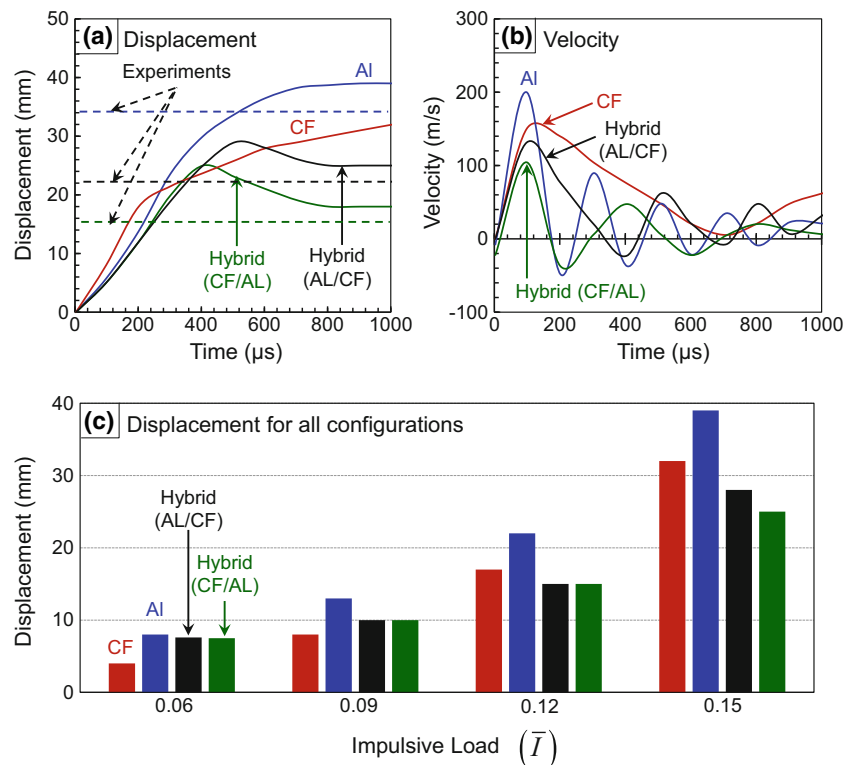

(a) Displacement

Experiments

Al

CF

Hybrid (CF/AL)

Hybrid (AL/CF)

(b) Velocity

Al

CF

Hybrid (AL/CF)

Hybrid (CF/AL)

(c) Displacement for all configurations

Hybrid (AL/CF)

Hybrid (CF/AL)

Al

CF

Impulsive Load $\left(\bar{I}\right)$

Fig. 16 Computational results for (**a**) reaction force and (**b**) transmitted impulse as functions of time; and (**c**) peak transmitted impulses for different structures and incident impulsive loads
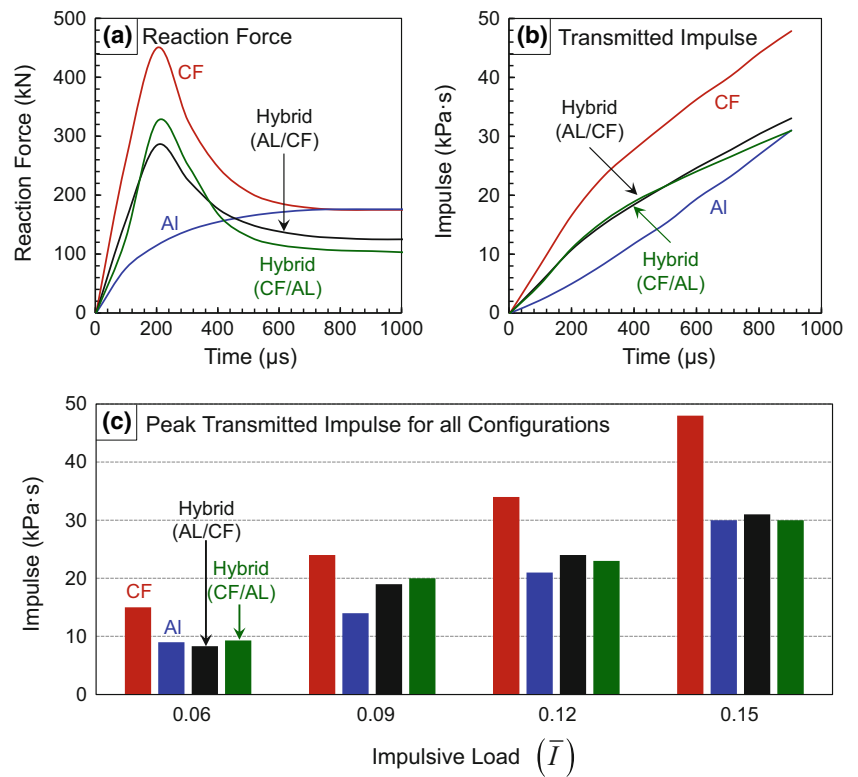
is responsible for ~60 %, the interfacial damage dissipation is responsible for ~25 % and in-ply damage dissipation is responsible for ~15 % of the total energy dissipation respectively. In the hybrid (CF/AL) plate, the aluminum section is responsible for

~50 %, the interfacial damage dissipation is responsible for ~30 % and in-ply damage dissipation is responsible for ~20 % of the total energy dissipation. It should be noted that the energy dissipation of the hybrid plates is slightly enhanced by an

Fig. 17 Computational results for energy dissipation histories for different components of (**a**) aluminum; (**b**) composite; (**c**) hybrid (AL/CF); and (**d**) hybrid (CF/AL) plates
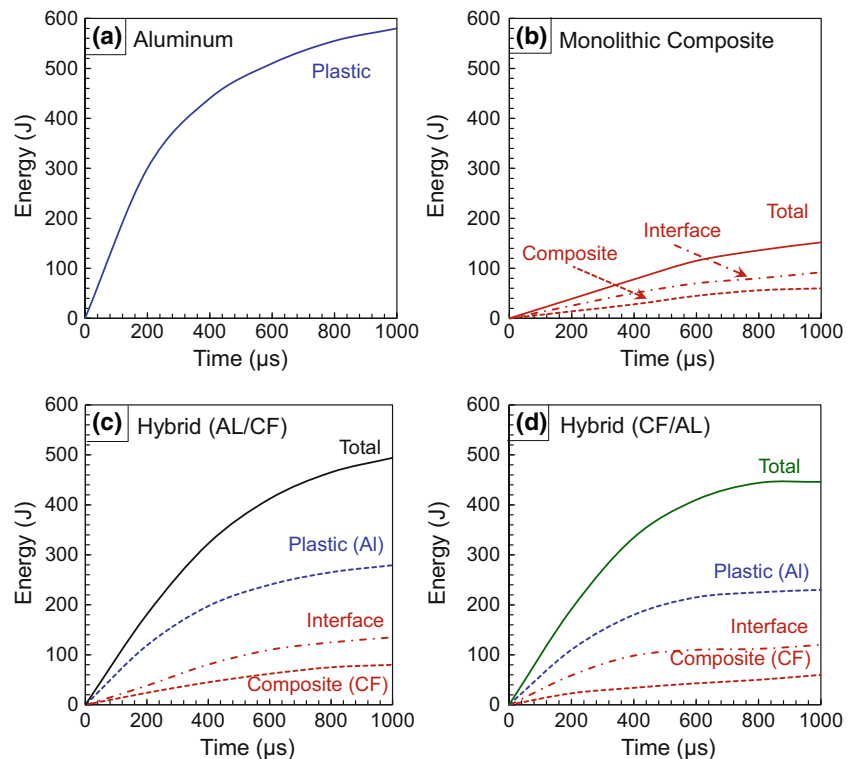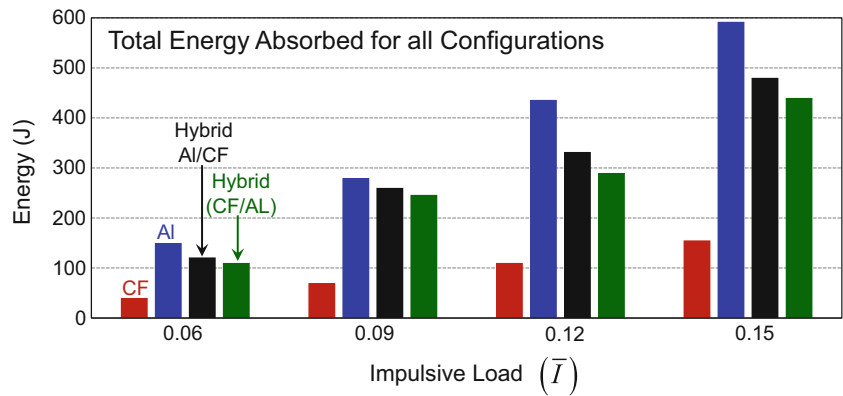
Fig. 18 Computational results for total energy dissipation for aluminum, carbon-fiber/epoxy, hybrid (AL/CF) and hybrid (CF/AL) plates

additional layer of adhesives required to bond the aluminum and composite sections. The comparison of total dissipated energy for different structural configurations subjected to a range of incident impulses is shown in Fig. 18. The monolithic aluminum plate dissipates the highest amount of energy for all load intensities while both the (AL/CF) and (CF/AL) hybrid plates dissipate ~75 % of the energy dissipated by the monolithic aluminum plates. Additionally, the (CF/AL) hybrid plates exhibit lower energy dissipation in both the aluminum and composite sections in comparison to the (AL/CF) hybrid plate. The monolithic composite plates are relatively inefficient with respect to energy dissipation capacity.

Design of hybrid structures for blast mitigation

To fully utilize the potential of hybrid metal composite structures, one consideration is to maximize the performance under a given load condition while maintaining or minimizing the mass. Weight-efficient designs of blast-resistant structures are determined by a number of factors, such as the expected incident load, types of materials, stacking sequences, interfacial effects, structural geometry and loading configuration. To quantify the effect of these factors on deformation response, a performance metric consisting of out-of-plane deflection, transmitted impulse, plastic dissipation and plastic dissipation density is developed.

Experiments and simulations discussed previously have revealed that hybrid structures perform marginally better than monolithic structures at low incident load intensities but exhibit superior blast resistance at higher load intensities where damage and failure play a major role. The stacking sequence consisting of composite on the impulse side and aluminum on the opposite side (CF/AL) provides the highest blast mitigation through a combination of minimum deflection and impulse transmission and maximum energy dissipation among the structures analyzed. It should be noted that the hybrid plates studied consist of equal weight of aluminum and carbon-fiber/epoxy laminate.

It is important to understand the role of hybrid plate construction and the effects of varying amounts of aluminum and carbon-fiber/epoxy in the design. A computational study is carried out by varying the percentage of aluminum in the (CF/AL) hybrid plate while the total mass is kept constant. The percentage of aluminum is varied from 0 % to 100 % in increments of 20 % and the remaining mass in each case is that of carbon-fiber/epoxy. Table 6 shows the mass and thickness of each section of the hybrid plate in the optimization analysis. The six hybrid plates consisting of varying amounts of aluminum are then subjected to loading under the four different incident impulse levels in Fig. 3(a-d).

Figure 19(a) shows the time histories of the out-of-plane deflection at the center of (CF/AL) hybrid plates with varying amounts of aluminum subjected to $\bar{I}=0.09$. The plate with 0 %

Table 6 Hybrid structures with different amounts of aluminum and carbon-fiber/epoxy studied

Plate Designation	AL Percentage	AL Thickness (mm)	AL Mass (kg)	CF/Epoxy Mass (kg)	CF/Epoxy Thickness (mm)
100 % AL	100	1	2.7	0	0
80 % AL	80	0.8	2.16	0.54	0.36
60 % AL	60	0.6	1.62	1.08	0.72
40 % AL	40	0.4	1.08	1.62	1.08
20 % AL	20	0.2	0.54	2.16	1.44
0 % AL	0	0	0	2.7	1.8

Fig. 19 Computational results for (**a**) out-of-plane displacement as a function of time and (**b**) peak out-of-plane displacement as a function of the percentage of aluminum in (CF/AL) hybrid plates for different incident impulse levels
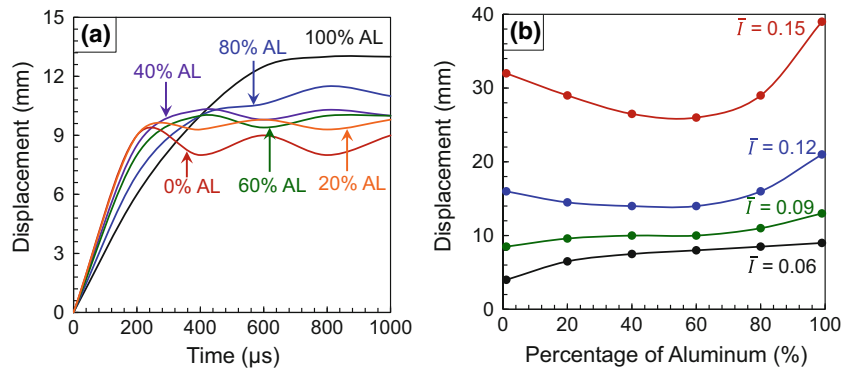

Al experiences high initial rate of deflection increase followed by vibration. As the amount of aluminum increases, the vibration diminishes, with the 100 % Al plate reaching a non-deforming state at approximately $t=700$ μs. Figure 19(b) shows the permanent deflection of the (CF/AL) hybrid plates as a function of the percentage of Al for a range of load magnitude. At low impulse magnitudes ($\bar{I} \leq 0.09$), the composite plate experiences the least deflection, with the permanent deflection increasing with the amount of aluminum. At higher impulse magnitudes ($\bar{I} > 0.09$) where fracture and failure are a major consideration, the plate with 60 % Al and 40 % carbon-fiber/epoxy composition (denoted as 60 % Al) exhibits the lowest deflection, undergoing 15 % and 25 % of the deflections experienced by the 0 % Al and 100 % Al plates, respectively. The 40 % Al plate experiences slightly higher deflections compared with the 60 % Al plate.

Minimizing the impulse transmitted to the downstream section is important for protecting the internal components of marine vessels. The magnitude of the transmitted impulse is therefore an important parameter concerning the blast resistance of composite structures. Clearly, the structure that transmits the least impulse at the lowest rate is most desirable. Figure 20(a) shows the reaction forces measured at supports and Fig. 20(b) shows the corresponding impulses transmitted through (CF/AL) hybrid plates consisting of varying amounts of aluminum subjected to $\bar{I}=0.09$. For the 0 % Al plate which is exclusively constructed from carbon-fiber/epoxy, the reaction forces show a sharp initial peak which subsides after

600 μs. As the amount of aluminum in the hybrid plate increases, the magnitude of the initial peak gradually decreases until it disappears at 100 % Al. Overall, the 0 % Al plate transmits the highest impulse while the 100 % Al plate transmits the least impulse. Figure 21 shows the transmitted impulses for the hybrid plates as a function of the percentage of aluminum for a range of incident impulse magnitude. The monolithic aluminum (100 % Al) plate transmits the least impulse at all load intensities while the 80 % Al and 60 % Al plates transmit 105 % and 110 % of the impulse transmitted by the 100 % Al plate, respectively. The results indicate that there is a minor benefit in terms of impulse mitigation in hybrid plates beyond a 40 % aluminum/ 60 % carbon-fiber/epoxy composition.

A drawback of composite structures is their significantly lower energy dissipation capacity relative to metallic structures. As discussed previously, composite plates dissipate ~15 % of the energy dissipated by monolithic aluminum plates of equal mass. Within the composite plates, adhesives and interfacial effects account for a majority of the inelastic dissipation while in-ply damage mechanisms account for a relatively minor fraction of the energy dissipated. Additionally, in hybrid structures, aluminum sections are responsible for a large fraction of total dissipated energy. An analysis of failure modes reveals the tendency of composite structures to experience fragmentation and failure under high intensity loads. Hybrid structures serve to eliminate this drawback and provide improved blast mitigation by enhancing the energy

Fig. 20 Computational results for (**a**) reaction force and (**b**) transmitted impulse as functions of time for (CF/AL) hybrid plates with varying amounts of aluminum
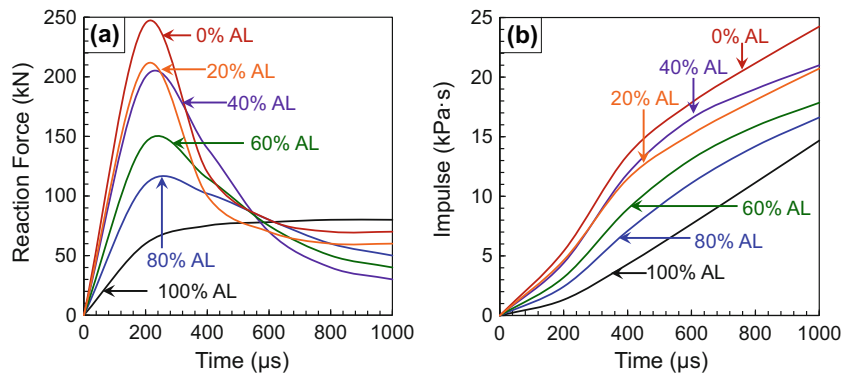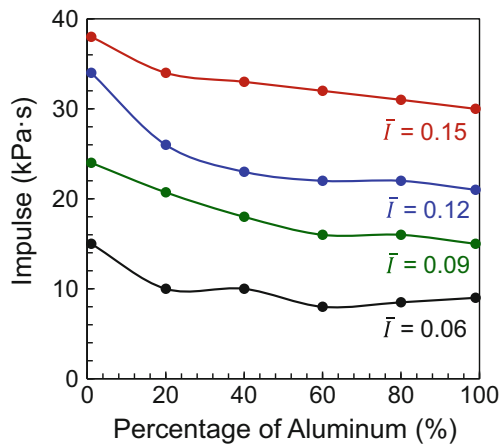
Fig. 21 Computational results for transmitted impulse as a function of the percentage of aluminum in (CF/AL) hybrid plates for different incident impulsive loads

dissipation capacity of the structures. Figure 22(a) shows the time histories of plastic dissipation in hybrid plates consisting of different amounts of aluminum while Fig. 22(b) shows the dissipation in hybrid plates as a function of the percentage of aluminum for a range of incident loads. The energy dissipated in the hybrid plates increases rapidly with the amount of aluminum up to 60 % and plateaus beyond that level. In fact, there is a slight decrease in dissipation for the 80 % Al -and 100 % Al plates at the lower load intensities. To evaluate the efficiency of energy dissipation in the hybrid plates, the ratio between the plastic dissipation in the aluminum to the mass of aluminum is calculated. This ratio, called dissipation density (dissipation per unit mass), is shown in Fig. 23(a) as a function of time for the (CF/AL) hybrid plates with varying amounts of aluminum and shown in Fig. 23(b) as a function of the percentage of aluminum in the hybrid plates. The results reveal that the dissipation per unit mass is highest for thin layers of aluminum in the 20 % Al and 40 % Al plates and decreases drastically as the percentage of aluminum increases.

It should be noted that the presence of the aluminum section in a hybrid plate has two main effects: (1) providing confinement for the carbon-fiber/epoxy plate to prevent shear cracking and fragmentation and (2) enhancing impact resistance by improving energy dissipation. The results reported

here show that these two effects require conflicting structural modifications. The first effect is best achieved by the presence of a thick aluminum layer while the second effect is best achieved by multiple thin aluminum layers. The design of the aluminum section thickness must then balance these two competing requirements. Further studies on this should explore the effects of stacking sequence involving alternating layers of carbon-fiber/epoxy and aluminum sections in a (CF/AL) configuration.

Concluding remarks

Marine structures must balance strength and load-carrying capacity with the ability to minimize impulse transmission for high blast and impact resistance. The combined experimental and computational research reported here is an attempt to quantify the underwater blast response of hybrid fiber-metal laminates with different stacking sequences under a range of incident impulsive loads. The peak pressures of the incident impulses considered range from 59 MPa to 198 MPa. Since all plates considered fail under an incident impulse of $\bar{I} = 0.15$ with a peak pressure of 198 MPa, this is the highest impulse intensity discussed in this paper. The experiments reported here are supported by fully dynamic 3D finite element calculations. The results from numerical calculations provide a more in-depth understanding of temporal and spatial evolution of different deformation modes in the structures and the partitioning of energy in different components.

The monolithic aluminum plates experience petalling failure and exhibit bulging and tensile necking in the central region under a range of incident impulsive loads. Composite plates undergo extensive delamination at all load intensities and experience in-ply damage in the form of matrix cracking, fiber cracking and fiber-matrix debonding. The failure is predominantly near the clamped boundary, indicating significant shear dependence of damage. The hybrid (AL/CF) plates exhibit bulging and tensile failure in the aluminum sections and large-scale shear cracking in the composite sections. Additionally, the lack of confinement for the composite plate

Fig. 22 Computational results for (**a**) plastic dissipation as a function of time and (**b**) plastic dissipation as a function of the percentage of aluminum in (CF/AL) hybrid plates for different incident impulsive
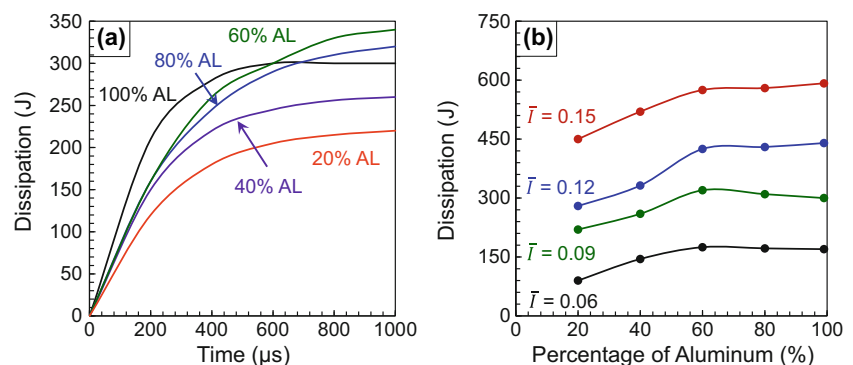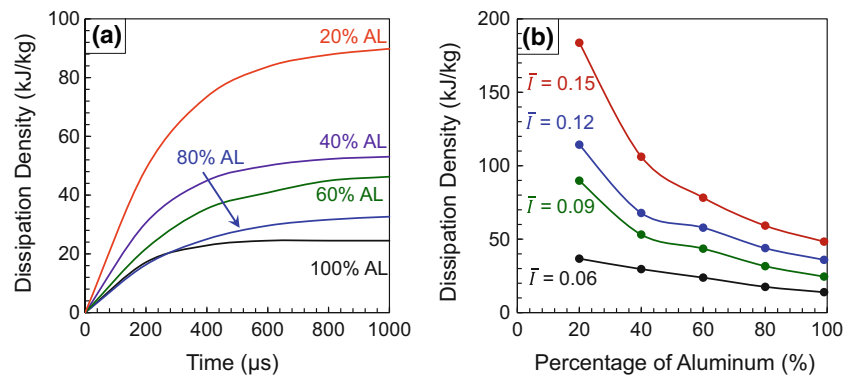
Fig. 23 Computational results for (**a**) plastic dissipation density as a function of time and (**b**) plastic dissipation density as a function of the percentage of aluminum in (CF/AL) hybrid plates for different incident impulsive loads

creates large delamination at the interface between the aluminum and composite sections. Conversely, the hybrid (CF/AL) plates exhibit significantly superior blast resistance with minimal shear cracking in the composite section and significantly lower bulging in the aluminum section. This behavior can be attributed to the confining conditions created by the aluminum section that prevents the composite from deflecting and failing under shear loads in conjunction with the stiff composite section which prevents excessive bulging. Both hybrid structures exhibit superior blast resistance in comparison to monolithic plates of equivalent mass.

With respect to the hybrid plates, it is determined that the stacking sequence consisting of the composite section in contact with water and aluminum section on the opposite side provides marginally higher blast mitigation capability. In stacking sequence, the carbon fiber composite section prevents the out-of-plane bulging in the aluminum section while the aluminum section prevents shear cracking in the carbon fiber composite section resulting in a symbiotic effect that enhances blast mitigation at all loading intensities while reducing delamination between the two sections.

The blast resistance of each plate is evaluated by comparing the impulses transmitted through and the energy dissipated by the plate. The hybrid structures are found to possess superior impulse mitigation capabilities at all impulsive loads, transmitting ~60 % of the impulses transmitted by the composite laminates. The monolithic aluminum plates and the aluminum sections of the hybrid plates are responsible for the majority of the energy dissipation at all impulse intensities, absorbing more than 60 % of the total energy dissipated in the hybrid plates. Interfacial damage dissipation is found to exceed in-ply damage dissipation in the composite sections. Overall, the hybrid metal/composite structures constitute better alternatives to monolithic structures of either material, due to the combination of high stiffness and strength-to-weight ratio.

In the hybrid plates, the composite section is responsible for restricting the out-of-plane deflection while the aluminum section plays a vital role in impulse mitigation and energy dissipation. It is found that that plates with 40 %-60 % of aluminum by weight provide an optimal combination of resistance to deflection, impulse mitigation and energy dissipation. Additionally, thinner layers of aluminum lead more efficient energy dissipation on a unit mass basis.

A parametric study is carried to quantify deflection, impulse transmission and energy dissipation as functions of incident load, material properties, and structural attributes. The insight gained provides guidelines for the design of next generation structures and retro-fitting of existing structures for which response to water-based impulsive loading is an important consideration. The exploration of different stacking sequences, adhesive strengths, relative thicknesses and inclusion of low density cellular solids for enhanced blast mitigation should form the basis of future studies.

References

1. Hudson GE (1951) A theory of the dynamic plastic deformation of a thin diaphragm. J Appl Phys 22:1–11
2. Wang AJ, Hopkins HG (1954) On the plastic deformation of built-in circular plates under impulsive load. J Mech Phys Solids 3:22–37
3. Menkes SB, Opat HJ (1973) Broken beams - tearing and shear failures in explosively loaded clamped beams. Exp Mech 13:480–486
4. Nurick GN, Shave GC (1996) The deformation and tearing of thin square plates subjected to impulsive loads - An experimental study. Int J Impact Eng 18:99–116
5. Lee YW, Wierzbicki T (2005) Fracture prediction of thin plates under localized impulsive loading. Part I: dishing. Int J Impact Eng 31:1253–1276
6. Wierzbicki T, Bao YB, Lee YW, Bai YL (2005) Calibration and evaluation of seven fracture models. Int J Mech Sci 47:719–743
7. Balden VH, Nurick GN (2005) Numerical simulation of the post-failure motion of steel plates subjected to blast loading. Int J Impact Eng 32:14–34

8. Kazemahvazi S, Radford D, Deshpande VS, Fleck NA (2007) Dynamic failure of clamped circular plates subjected to an underwater shock. J Mech Mater Struct 2:2007–2023

9. Steeves CA, Fleck NA (2004) Collapse mechanisms of sandwich beams with composite faces and a foam core, loaded in three-point bending. Part II: experimental investigation and numerical modelling. Int J Mech Sci 46:585–608

10. Tagarielli VL, Deshpande VS, Fleck NA (2007) The dynamic response of composite sandwich beams to transverse impact. Int J Solids Struct 44:2442–2457

11. Schubel PM, Luo JJ, Daniel IM (2007) Impact and post impact behavior of composite sandwich panels. Compos Part a-Appl S 38:1051–1057

12. Nemes JA, Simmonds KE (1992) Low-velocity impact response of foam-core sandwich composites. J Compos Mater 26:500–519

13. Mines RAW, Worrall CM, Gibson AG (1994) The static and impact behavior of polymer composite sandwich beams. Composites 25:95–110

14. I.M.D. J. L. Abot (2001) Composite sandwich beams under low velocity impact, Proc. of AIAA Conf., Seattle

15. Schubel PM, Luo JJ, Daniel IM (2005) Low velocity impact behavior of composite sandwich panels. Compos Part a-Appl S 36:1389–1396

16. Abrate S (1991) Impact on laminated composite materials. Appl Mech Rev 44(4):155–190

17. Abrate S (1994) Impact on laminated composites: recent advances. Appl Mech Rev 47:517–544

18. Joshi SP, Sun CT (1985) Impact induced fracture in a laminated composite. J Compos Mater 19:51–66

19. Chang FK, Choi HY, Jeng ST (1990) Study on impact damage in laminated composites. Mech Mater 10:83–95

20. Chang FK, Choi HY, Jeng ST (1990) Characterization of impact damage in laminated composites. Sampe J 26:18–25

21. Lessard LB, Chang FK (1991) Damage tolerance of laminated composites containing an open hole and subjected to compressive loadings.2. Experiment. J Compos Mater 25:44–64

22. Cantwell WJ, Morton J (1991) The impact resistance of composite-materials - a review. Composites 22:347–362

23. Hashin Z (1986) Analysis of stiffness reduction of cracked cross-ply laminates. Eng Fract Mech 25:771–778

24. Hashin Z (1987) Analysis of orthogonally cracked laminates under tension. J Appl Mech-T Asme 54:872–879

25. Minnaar K, Zhou M (2004) A novel technique for time-resolved detection and tracking of interfacial and matrix fracture in layered materials. J Mech Phys Solids 52:2771–2799

26. Espinosa HD, Lee S, Moldovan N (2006) A novel fluid structure interaction experiment to investigate deformation of structural elements subjected to impulsive loading. Exp Mech 46:805–824

27. Latourte F, Gregoire D, Zenkert D, Wei XD, Espinosa HD (2011) Failure mechanisms in composite panels subjected to underwater impulsive loads. J Mech Phys Solids 59:1623–1646

28. Wei XD, de Vaucorbeil A, Tran P, Espinosa HD (2013) A new rate-dependent unidirectional composite model - Application to panels subjected to underwater blast. J Mech Phys Solids 61:1305–1318

29. McShane GJ, Stewart C, Aronson MT, Wadley HNG, Fleck NA, Deshpande VS (2008) Dynamic rupture of polymer-metal bilayer plates. Int J Solids Struct 45:4407–4426

30. Dharmasena KP, Wadley HNG, Xue ZY, Hutchinson JW (2008) Mechanical response of metallic honeycomb sandwich panel structures to high-intensity dynamic loading. Int J Impact Eng 35:1063–1074

31. Battley M, Allen T (2012) Servo-hydraulic system for controlled velocity water impact of marine sandwich panels. Exp Mech 52:95–106

32. Battley M, Stenius I, Breder J, Edinger S (2005) Dynamic characterisation of marine sandwich structures. Sandw Struct7: Adv Sandw Struct Mater 537–546

33. Tekalur SA, Bogdanovich AE, Shukla A (2009) Shock loading response of sandwich panels with 3-D woven E-glass composite skins and stitched foam core. Compos Sci Technol 69:736–753

34. Tekalur SA, Shukla A, Shivakumar K (2008) Blast resistance of polyurea based layered composite materials. Compos Struct 84:271–281

35. LeBlanc J, Shukla A, Rousseau C, Bogdanovich A (2007) Shock loading of three-dimensional woven composite materials. Compos Struct 79:344–355

36. Grogan J, Tekalur SA, Shukla A, Bogdanovich A, Coffelt RA (2007) Ballistic resistance of 2D and 3D woven sandwich composites. J Sandw Struct Mater 9:283–302

37. Wang EH, Gardner N, Shukla A (2009) The blast resistance of sandwich composites with stepwise graded cores. Int J Solids Struct 46:3492–3502

38. Avachat S, Zhou M (2015) High-speed digital imaging and computational modeling of dynamic failure in composite structures subjected to underwater impulsive loads. Int J Impact Eng 77:147–165

39. Vlot A (1996) Impact loading on fibre metal laminates. Int J Impact Eng 18:291–307

40. Yaghoubi AS, Liaw B (2013) Effect of lay-up orientation on ballistic impact behaviors of GLARE 5 FML beams. Int J Impact Eng 54:138–148

41. Yaghoubi AS, Liaw B (2014) Influences of thickness and stacking sequence on ballistic impact behaviors of GLARE 5 FML plates: Part II - Numerical studies. J Compos Mater 48:2363–2374

42. Yaghoubi AS, Liaw B (2014) Influences of thickness and stacking sequence on ballistic impact behaviors of GLARE 5 FML plates: Part I-experimental studies. J Compos Mater 48:2011–2021

43. Fatt MSH, Lin CF, Revilock DM, Hopkins DA (2003) Ballistic impact of GLARE (TM) fiber-metal laminates. Compos Struct 61:73–88

44. Abdullah MR, Cantwell WJ (2012) The high-velocity impact response of thermoplastic-matrix fibre-metal laminates. J Strain Anal Eng 47:432–443

45. Fan J, Guan ZW, Cantwell WJ (2011) Numerical modelling of perforation failure in fibre metal laminates subjected to low velocity impact loading. Compos Struct 93:2430–2436

46. Langdon GS, Lemanski SL, Nurick GN, Simmons MC, Cantwell WJ, Schleyer GK (2007) Behaviour of fibre-metal laminates subjected to localised blast loading: Part I - experimental observations. Int J Impact Eng 34:1202–1222

47. Lemanski SL, Nurick GN, Langdon GS, Simmons MC, Cantwell WJ, Schleyer GK (2007) Behaviour of fibre metal laminates subjected to localised blast loading - Part II: quantitative analysis. Int J Impact Eng 34:1223–1245

48. Vo TP, Guan ZW, Cantwell WJ, Schleyer GK (2013) Modelling of the low-impulse blast behaviour of fibre-metal laminates based on different aluminium alloys. Compos Part B-Eng 44:141–151

49. Vo TP, Guan ZW, Cantwell WJ, Schleyer GK (2012) Low-impulse blast behaviour of fibre-metal laminates. Compos Struct 94:954–965

50. Karagiozova D, Langdon GS, Nurick GN, Yuen SCK (2010) Simulation of the response of fibre-metal laminates to localised blast loading. Int J Impact Eng 37:766–782

51. Langdon GS, Nurick GN, Karagiozova D, Cantwell WJ (2010) Fiber-metal laminate panels subjected to blast loading. Dyn Fail Mater Struct 269–296

52. Wei XD, Tran P, de Vaucorbeil A, Ramaswamy RB, Latourte F, Espinosa HD (2013) Three-dimensional numerical modeling of composite panels subjected to underwater blast. J Mech Phys Solids 61:1319–1336

53. Avachat S, Zhou M (2011) Effect of facesheet thickness on dynamic response of composite sandwich plates to underwater impulsive loading. Exp Mech 52:83–93

54. Avachat S, Zhou M (2011) Dynamic response of composite sandwich structures subjected to underwater impulsive loads: experiments and simulations conference proceedings of the 16th international conference on composite structures, ICCS-16, Ferreira AJM (ed), FEUP, Porto, 2011

55. Avachat S, Zhou M (2010) Dynamic response of submerged composite sandwich structures to blast loading, proceedings of the IMPLAST 2010 - SEM fall conference, October 12–14 2010 providence. Arun Shukla (Editor), Rhode Island, USA

56. Swisdak MM (1978) Explosion effects and properties: Part II – explosion effects in water. Technical Report, Naval Surface Weapons Center, Dahlgren, Virginia, USA

57. Taylor GI (1941) The pressure and impulse of submarine explosion waves on plates., The scientific papers of G I Taylor, vol. III. Cambridge University Press, Cambridge, pp 287–303

58. Arora H, Kelly M, Worley A, Del Linz P, Fergusson A, Hooper PA, Dear JP (2014) Compressive strength after blast of sandwich composite materials, Philosophical Transactions of the Royal Society a-Mathematical Physical and Engineering Sciences, 372

59. Arora H, Hooper PA, Dear JP (2012) The effects of air and underwater blast on composite sandwich panels and tubular laminate structures. Exp Mech 52:59–81

60. Taylor GI (1963) The Scientific Papers of G I Taylor. Cambridge University Press, Cambridge

61. Kambouchev N, Radovitzky R, Noels L (2007) Fluid–structure interaction effects in the dynamic response of free-standing plates to uniform shock loading. J Appl Mech-T Asme 74:1042–1045

62. Hutchinson JW (2009) Energy and momentum transfer in air shocks. J Appl Mech-T Asme 76

63. Cole RH (1947) Spherical shock waves from underwater explosions. Phys Rev 72:177

64. Kambouchev N, Noels L, Radovitzky R (2007) Numerical simulation of the fluid–structure interaction between air blast waves and free-standing plates. Comput Struct 85:923–931

65. Johnson GR, Cook WH (1985) Fracture characteristics of 3 metals subjected to various strains. strain rates, temperatures and pressures. Eng Fract Mech 21:31–48

66. Raftenberg MN (2001) A shear banding model for penetration calculations. Int J Impact Eng 25:123–146

67. Corbett BM (2006) Numerical simulations of target hole diameters for hypervelocity impacts into elevated and room temperature bumpers. Int J Impact Eng 33:431–440

68. Hashin Z (1980) Failure criteria for unidirectional fiber composites. J Appl Mechanics-Trans Asme 47:329–334

69. Hibbit, Karlsson, Sorensen (2009) Abaqus/explicit user's manual, version 6.9

70. Lapczyk I, Hurtado JA (2007) Progressive damage modeling in fiber-reinforced materials. Compos Part a-Appl S 38:2333–2341

71. Chan S, Fawaz Z, Behdinan K, Amid R (2007) Ballistic limit prediction using a numerical model with progressive damage capability. Compos Struct 77:466–474

72. Pinho ST, Robinson P, Iannucci L (2006) Fracture toughness of the tensile and compressive fibre failure modes in laminated composites. Compos Sci Technol 66:2069–2079

73. Needleman A (1990) An analysis of tensile decohesion along an interface. J Mech Phys Solids 38:289–324

74. Tvergaard V, Hutchinson JW (1992) The Relation between Crack-Growth Resistance and Fracture Process Parameters in Elastic Plastic Solids. J Mech Phys Solids 40:1377–1397

75. Tvergaard V, Needleman A (1992) Effect of crack meandering on dynamic. Ductile fracture. J Mech Phys Solids 40:447–471

76. Needleman A, Tvergaard V (1994) Mesh effects in the analysis of dynamic ductile crack-growth. Eng Fract Mech 47:75–91

77. Xu XP, Needleman A (1994) Numerical simulations of fast crack-growth in brittle solids. J Mech Phys Solids 42:1397

78. Camacho GT, Ortiz M (1996) Computational modelling of impact damage in brittle materials. Int J Solids Struct 33:2899–2938

79. Espinosa HD, Zavattieri PD, Dwivedi SK (1998) A finite deformation continuum discrete model for the description of fragmentation and damage in brittle materials, in, Pergamon-Elsevier Science Ltd, pp. 1909–1942

80. Camanho PP, Davila CG, de Moura MF (2003) Numerical simulation of mixed-mode progressive delamination in composite materials. J Compos Mater 37:1415–1438

81. Minnaar K, Zhou M (2002) Characterization of impact in composite laminates. AIP Conf Proc 620:1208

82. Zhai J, Zhou M (2000) Finite element analysis of micromechanical failure modes in a heterogeneous ceramic material system. Int J Fracture 101:161–180

83. Benzeggagh ML, Kenane M (1996) Measurement of mixed-mode delamination fracture toughness of unidirectional glass/epoxy composites with mixed-mode bending apparatus. Compos Sci Technol 56:439–449

84. Abell AB, Lange DA (1998) Fracture mechanics modeling using images of fractured surfaces. Int J Solids Struct 35:4025–4033

85. Gullerud AS, Gao XS, Dodds RH, Haj-Ali R (2000) Simulation of ductile crack growth using computational cells: numerical aspects. Eng Fract Mech 66:65–92

86. Pijaudier-Cabot G, Bazant ZP (1987) Nonlocal Damage Theory. J Eng Mech 113:1512–1533

87. Comi C (2001) A non-local model with tension and compression damage mechanisms. Eur J Mech a-Solid 20:1–22